ORIGINAL PAPER

Experimental Study on the Movement and Failure Characteristics of Karst Mountain with Deep and Large Fissures Induced by Coal Seam Mining

Zhongping Yang[1,2,3] · Qian Zhao[1,2,3] · Xinrong Liu[1,2,3] · Zhiming Yin[1,4] · Yalong Zhao[1,2,3] · Xuyong Li[1,2,3]

Abstract

To investigate the temporal and spatial evolution process of overlying karst mountain instability caused by mining, the case of "8.28" mega landslide in Pusa, Nayong County, Guizhou Province, China, is taken as the example. Based on the results of the field investigation after the disaster, the complete process of rock strata fracture and slope instability under the descending and ascending mining conditions of gently inclined coal seam is reproduced by similitude model experiments. According to the key motion features of overburden deformation and fracture evolution law, the failure process of slope collapse controlled by deep and large karst fissures under mining action is summarized. And the change law of overburden pressure and displacement in the mining process is analyzed as well as the failure mode of slope collapse is proposed. The results show that the slope experiences four failure stages in the process of coal seam descending mining: coal seam roof caving, overburden cantilever tension fracture, overburden integral dumping subsidence and slope instability collapse, and the slope undergoes deformation toward the free surface and downward. During the ascending mining process, the slope experiences four failure stages: periodic caving of coal seam roof, upward transmission of separated fractures, overburden integral bending subsidence and slope instability collapse, and the slope undergoes deformation toward the inside of the slope and downward. The rock mass ahead of the advancing direction of working face has the phenomenon of tension–compression stress transformation. Along the mining direction, the overburden sequentially experiences the change process of pressure increase, decrease, or increase again, and stabilization. Deep and large karst fissures at the slope top are the structural basis for the occurrence of collapse. Coal mining activities have a certain promoting effect on mountain cracking and rock fragmentation. The failure mode of slope can be summarized as tension–shear–slip–toppling collapse failure. Improved understanding of the deformation movement characteristics and damage mode of slope can aid in early identification and timely warning of geo-hazards in karst area.

✉ Zhongping Yang
  yang-zhp@163.com

✉ Xinrong Liu
  liuxrong@126.com

1 School of Civil Engineering, Chongqing University, Chongqing 400045, China

2 State Key Laboratory of Coal Mine Disaster Dynamics and Control, Chongqing University, Chongqing 400044, China

3 National Joint Engineering Research Center for Prevention and Control of Environmental Geological Hazards in the TGR Area, Chongqing University, Chongqing 400045, China

4 School of Hydraulic and Ecological Engineering, Nanchang Institute of Technology, Nanchang 330099, China

Highlights

- This paper focuses on the deformation movement features and failure modes of mountains controlled by deep and large karst fissures under mining action.
- The full process of rock strata fracture and slope instability under descending and ascending mining conditions is reproduced in a simulated model.
- Extensive karst fissures at the slope top are the main structural basis for the occurrence of collapse.
- Coal mining activities have a certain promoting effect on mountain cracking and rock fragmentation.
- The failure mode of slopes can be summarized as tension-shear-slip-toppling collapse failure.

Keywords Underground mining · Karst slope · Fracture · Failure mode · Similitude model experiment

1 Introduction

The karst area in southwest China is characterized by complex geological structure, intense karstification and concentrated rainfall. Due to the special formation history of strata, the karst mountain area is generally characterized by topography and landform with steep top and gentle bottom, and strata structure with hard top and soft bottom (Xu et al. 2016; Chen et al. 2021). Under the long geological action, deep and large non-systematic karst fissures are developed in the slope body, which is one of the triggering factors of mining landslide (Singhal and Gupta 1999). A large number of engineering examples show that the occurrence of landslide disasters on rock mountains is often accompanied by the exploitation of underground mineral resources (Li et al. 2016; Ma et al. 2018; Fernández et al. 2020). The underground mining will cause the change of the original stress state of overburden and reduce the strength of the original weak structural surface, lead to the formation and development of mining cracks, and thus aggravating the deformation and failure process of mountain (Lana 2014; Salmi et al. 2017). Since the twentieth century, several incidents of slope movements caused by mining operations have occurred around the world, such as the Frank landslide in Albert, Canada in 1903 (Benko and Stead 1998), the Aberfan landslide in South Wales, UK in 1966 (Bentley and Siddle 1996), a rockfall avalanche in Nattai North, Australia in 1984 (Cunningham 1988), and the Dündar landslide in Bursa, Turkey in 2004 (Erginal et al. 2008). Typical mining landslides in China include the Jiguanling landslide in Wulong, Chongqing (He et al. 2018), the Jiwei Mountain landslide in Wulong, Chongqing (Feng et al. 2016), the Guanling landslide in Guizhou (Liu et al. 2015), the Zhenxiong landslide in Yunnan (Yin et al. 2013), and the rock avalanche in Pusa, Guizhou (Fan et al. 2019). The abovementioned mining landslide accidents are large in scale and serious in impact, all of which have caused major casualties or major secondary disasters.

With the continuous exploitation of natural resources, open-pit mines with slopes exceeding 200 m have become the most common type of open-pit mines in the world (Nie et al. 2015). In recent years, the implementation of field geological investigations, combined with physical model tests based on the survey results and numerical calculations, has become a more effective method for slope stability analysis (Wu et al. 2004; Scaringi et al. 2018; Hu et al. 2019; Do and Wu 2019, 2020a, b). When the similarity ratio is basically satisfied, the physical model test can truly reflect the movement characteristics of rock stratum and the evolution law of fractures, reproduce the complete process of rock rupture and rockfall shedding (Wang et al. 2019, 2020), and can comprehensively consider multiple factors e.g., precipitation (Capparelli et al. 2019), support reinforcement (Tangri and Rawat 2021) and vibration (Ghadafi et al. 2017). Most previous physical model tests focused on monitoring landslide mass displacement and evaluating slope displacement change (Zhang et al. 2018b), but neglected the changes in internal stresses during slope deformation and the influence of geological structures on the landslide process and failure modes. Only a few research results, such as Sun and Yao (1983), Zheng et al. (2015), emphasized the key role of geological structure and underground mining activities on the genesis of rock avalanches and rockfall. Tao et al. (2020) innovatively used "improved paraffin-graphite heat sensitive material" to simulate the structural plane, and designed a model-scale NPR (negative Poisson's ratio) anchor cable to monitor the attenuation change in the shear strength index of sliding floor when landslide occurs.

The most common triggering mechanisms of rock slope failure include rainfall, weathering, seismic events, volcanic activities and other environmental factors. The resulting failure processes have been well studied and proposed by many researchers (Wu et al. 2017; Eberhardt et al. 2005; Valentin et al. 2016; Sebastian et al. 2014). However, reports on the influence mechanism and deformation response of underground mining-induced landslides, as well as the failure

process and failure mode of mining landslides are often lack of systematic research or literature. In view of this, based on the case of "8.28" mega landslide in Pusa, Nayong County, Guizhou Province, China, this paper studies the overburden movement characteristics and fracture evolution law under different mining methods of gently inclined coal seam by means of geological survey, field investigation, and similar model test, analyzes the pressure and displacement change law overburden during mining, and proposes the failure process and failure mode of slope collapse controlled by deep and large karst fissures under the action of mining.

2 Geological Setting and Mining Activity

On August 28, 2017, at 10:30 a.m. (02:30 UTC), a large scale of mountain rock avalanche occurred in Pusa village, Zhangjiawan town, Nayong county, Guizhou Province, China (N26° 38′ 04.55″, E105° 26′ 56.14″). The rock mass with the volume of 49.1×10^4 m^3 moved down and scraped the original loose deposits and finally formed deposits of 82.3×10^4 m^3, which destroyed parts of Pusa village, resulted in the death of 26 persons, missing of nine persons (later confirmed dead) and injured of eight persons (Cui et al. 2022).

The Pusa landslide developed along a steep slope, with a ridge reaching 2147 m a.s.l. and the foot located at 1842 m a.s.l. The climate is subtropical and monsoon-influenced, with an average annual temperature of 13.6 °C. The annual precipitation is slightly over 1200 mm, with the rainfall process mostly occurring from May to September. Formations outcropping in the area include (i) the Quaternary (Q_4), consisting of very thin clay and sandy clay; (ii) the Yelang Formation of the Lower Triassic (T_1y), consisting of limestone, silty mudstone and argillaceous siltstone; (iii) the Changxing–Dalong Formation of the upper Permian ($P_2c + d$), consisting of silty mudstone, limestone, argillaceous siltstone and coal seams; and (iiii) the Longtan Formation of the upper Permian (P_2l), consisting of argillaceous siltstone, carbonaceous mud-stone and coal seams (Figs.1, 2). The Pusa landslide developed within the Yelang Formation on an anaclinal steepened slope extending toward N 40°–50° E, at
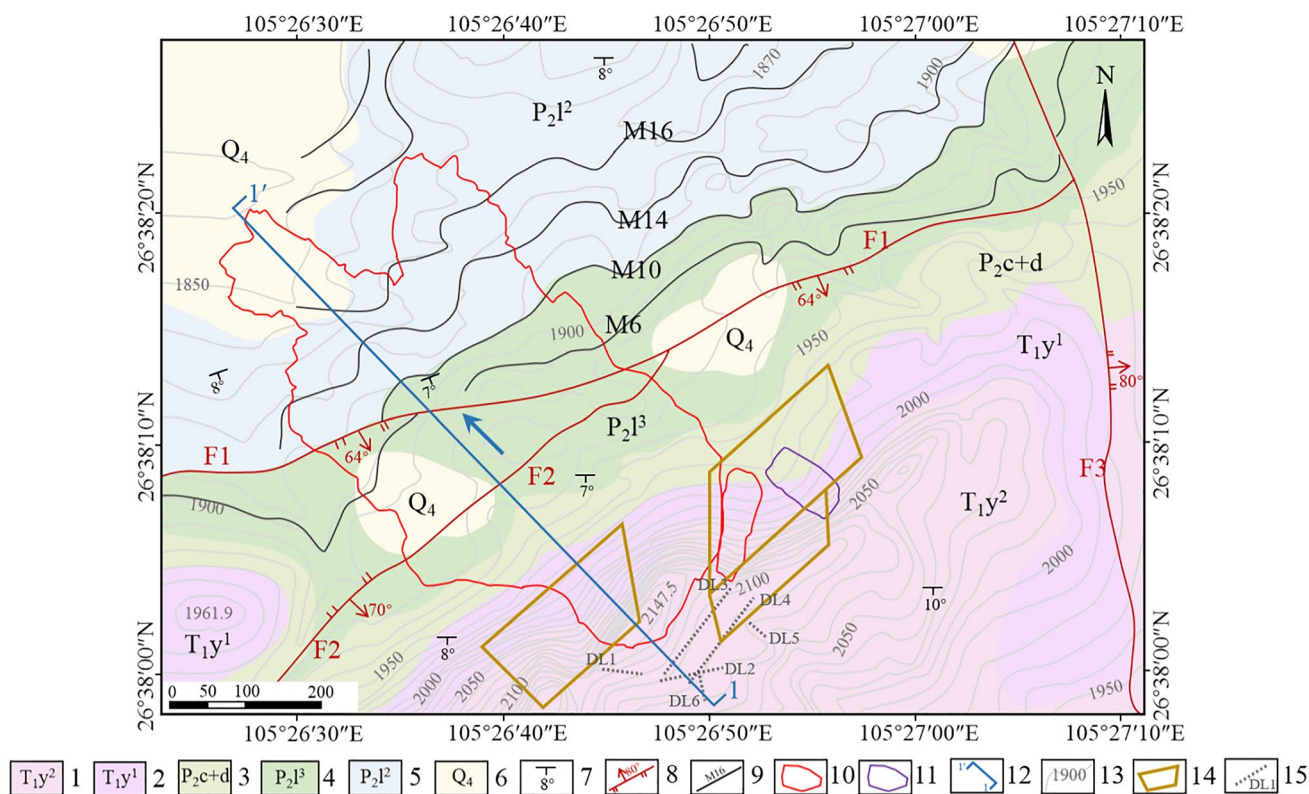

Fig. 1 Engineering geological map of the investigated area before the occurrence of the Pusa landslide: 1. Second member of the Yelang Formation of the Lower Triassic; 2. First member of the Yelang Formation of the Lower Triassic; 3. The Changxing–Dalong Formation of the upper Permian; 4. Third member of the Longtan Formation of the upper Permian; 5. Second member of the Longtan Formation of the upper Permian; 6. Quaternary deposits; 7. Rock stratum occurrence; 8. Fault; 9. Coal seam; 10. The outline of 8.28 Pusa landslide; 11. Historical collapse boundary; 12. Section line; 13. Contour line; 14. Goaf area; 15. Large crack
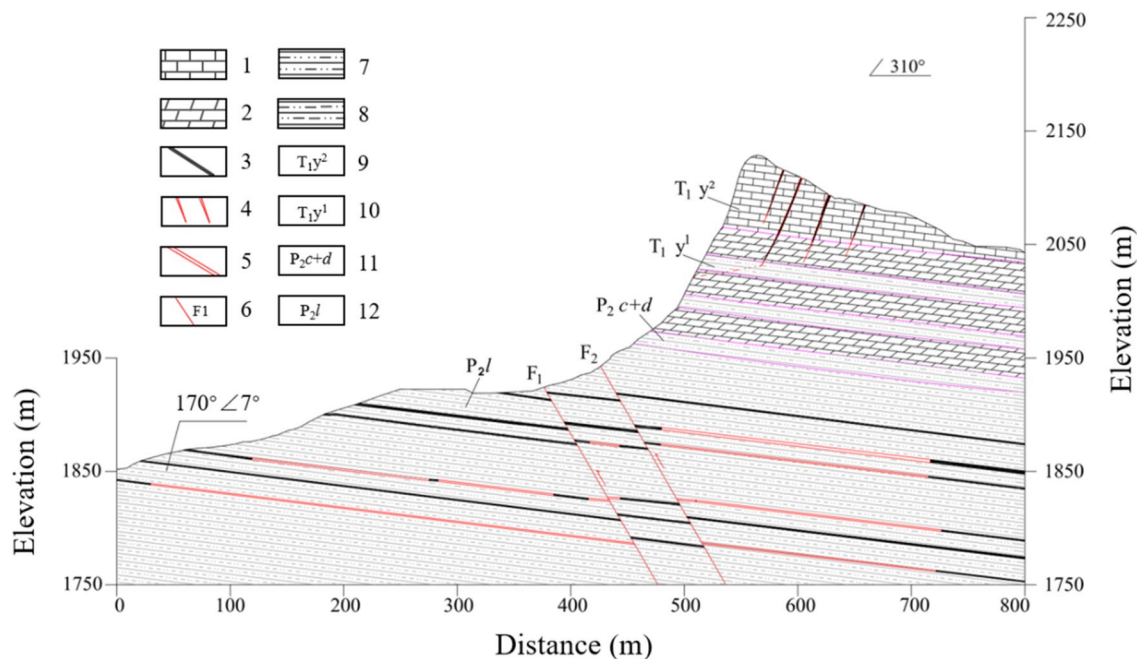
Fig. 2 Profile of the Pusa landslide along principal sliding direction (1–1′ in Fig. 1): 1. Limestone; 2. Mudstone; 3. Coal seam; 4. Deep and large karst fissures; 5. Goaf area; 6. Fault; 7. Muddy siltstone; 8. Silty mudstone; 9. Second member of the Yelang Formation of the Lower Triassic; 10. First member of the Yelang Formation of the Lower Triassic; 11. The Changxing–Dalong Formation of the upper Permian; 12. The Longtan Formation of the upper Permian. Collated from literature Yang et al. (2020)

Fig. 3 Typical erosion signs and rock structure at the rear edge of collapse source area: **a** the dissolution cavities; **b** the dissolution pipelines; **c** the dissolution fissures; **d** the rock mass on the steep cliff wall is cut into blocks by well-developed joints
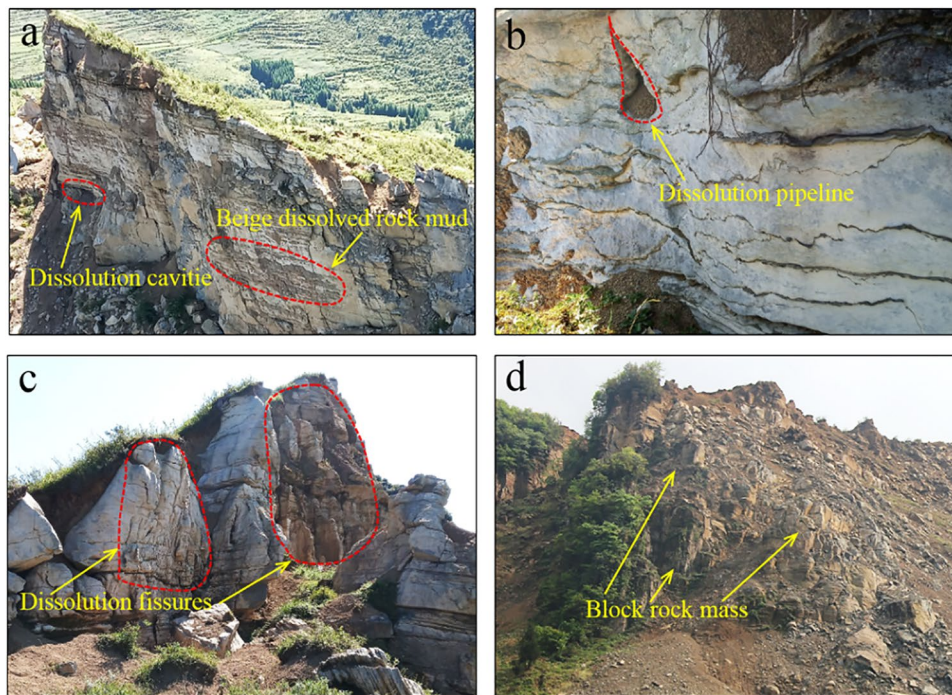
a location in which the strata gently dip inward with attitude N 80° E/SE∠5°–10°.

Usually below 1500 m is called low to medium altitude, and the study area features low to middle elevation mountainous landform with typical karst features, which displays severe signs of erosion. The limestone at the rear edge of the avalanche source area was strongly dissolved, covering its surface with a layer of beige dissolved rock mud.

The dissolution cavities, dissolution pipelines and dissolution fissures were clearly visible on the steep cliff wall, and limestone was often cut into separate blocks by well-developed joints (Fig. 3). The joints gaps were filled by debris, and the cementation degree between the broken block rock masses was very low, so the slope was very prone to local rockfall. At the shoulder of the slope (about 2110 m a.s.l), four groups of deep and large karst fissures were developed downward (Fig. 2), with depths ranging from 50 to 80 m and widths of 2–3 m. A large number of karst collapse pits were identified on the top of the slope at the back edge of the collapse area, among which the diameter of the largest collapse pit reached 5.2 m and the visible depth was about 2.1 m, and the exposed surface was Quaternary (Q4) residual slope deposits.

Three major faults (F1, F2, and F3) were identified in the area, as shown in Fig. 1. F1 and F2 developed below the scarp in the landslide source area, with a fault spacing of about 70 m, and F3 was found 400–500 m northeast of the slope. Since the coal seams between F1 and F2 had only been mined in small amounts, and the fault boundary retained the security coal pillar, the area between the two faults was equivalent to a long security pillar. The analysis shows that the coal seam mining on the left side of F1 has less influence on the slope, and the stability of the slope is mainly affected by the deep coal seam mining on the right side of F2. During the mining period of Pusa coal mine (from 1995 to 2017), no strong earthquake activity has been found in this area and the neighboring areas, and no earthquake indication that may affect the slope stability has been found before the collapse.

Mining occurred in six coal seams that developed in the Longtan Formation, which were M6, M10, M14, M16, M18 and M20 from top to bottom, with thickness of 2.01, 2.12, 1.23, 1.49, 0.37 and 0.84 m, respectively. The total thickness of coal seams was about 8.06 m, and the attitude of which was consistent with that of the strata. According to relevant mining information, Pusa coal mine mainly mined M20 and M16 from 1995 to 2012, and a large crack (DL1 and DL2 in Fig. 1) was identified behind the source area by Ouyang and Lan (2009) from September 2009 to December 2009. From 2013 to 2017, M14 and M10 were mined, with M6 presumably being partially mined. During this period, the cracks in the rear of the source area continued to expand to form subsidence troughs (DL3 and DL4 in Fig. 1), and occasionally small collapses occurred on the slope surface. It is believed that there is a certain time correspondence and causal relationship between the tension cracks behind the source area and the mining of M14 and M10 (Zhong et al. 2020). The coal mine finally ceased production on August 24, 2017, at which time the lower coal seam of the slope was basically mined. The goaf formed by the coal seam mining is shown in Fig. 2.

3 Study Methodology

3.1 Field Investigation and Analysis

From the results of the field investigation and analysis, the Pusa landslide can be generally divided into two parts: major sliding areas (zone A–E) and the landslide-affected surrounding areas (zone I–III) (Fig. 4).

The top elevation of source area (zone A) was 2080–2100 m a.s.l., and the lower shear outlet was roughly at about 2000 m a.s.l. This zone was about 85 m high, 145 m wide and 40 m thick. The strike angle of the scarp is about N 40° E, and the stratum is inclined inward (attitude N 80° E–EW/SE∠5–7°).

Track-abrasion area (zone B), about 180 m wide and 80 m long, spans from about 2000 m a.s.l. to about 1930 m a.s.l. The landslide mass scraped the loose deposits on the slope surface, early rockfall sediments and a small amount of bedrock, resulting in an average erosion of about 1.5 m on the slope surface, with a shovel-scraped volume of about 2.1×10^4 m^3.

Deposition area (zone C) was originally a relatively open, gentle sloping area with an overall slope of about 10°–15°. The surface was a soft tillage layer with an estimated thickness of about 2 m. The landslide scraped and pushed most of the soil down to the front edge of the deposition area, and the movement direction of the debris flow was changed due to the blocking effect of some houses. The area morphology was finger-like extension (Fig. 1), its average longitudinal length was about 575 m, width was about 360 m, and the shovel-scraped volume was about 31×10^4 m^3. A large quantity of fragmented siltstone and marls were scattered in the deposition area with many large size blocks reaching a maximum grain size of 16.6 m.

The rock mass on the north side of the source area (zone D) occurred a small collapse while the main body was deformed. The length of the collapse area was about 140 m, the transverse width was 50–70 m, the average thickness was about 2 m, and the volume was $1.4–1.9 \times 10^4$ m^3. In zone E, a small collapse occurred in 2016, involving a volume of $0.7–1 \times 10^4$ m^3.

After the landslide event, tensile fractures with strike angle of 35° were found in the unstable rock mass in the rear part (zone I), the largest of which was a 180 m long trough, about 12 m deep and up to 30 m wide. The southern side remained bound to the bedrock, where a series of tensile radial cracks were developed. Overall stability in the region seems poor.

Unstable rock mass on the north flank (zone II) was located just behind zone D and E, up to an elevation of 2100 m a.s.l. Here, a large fracture developed, 31 m long,
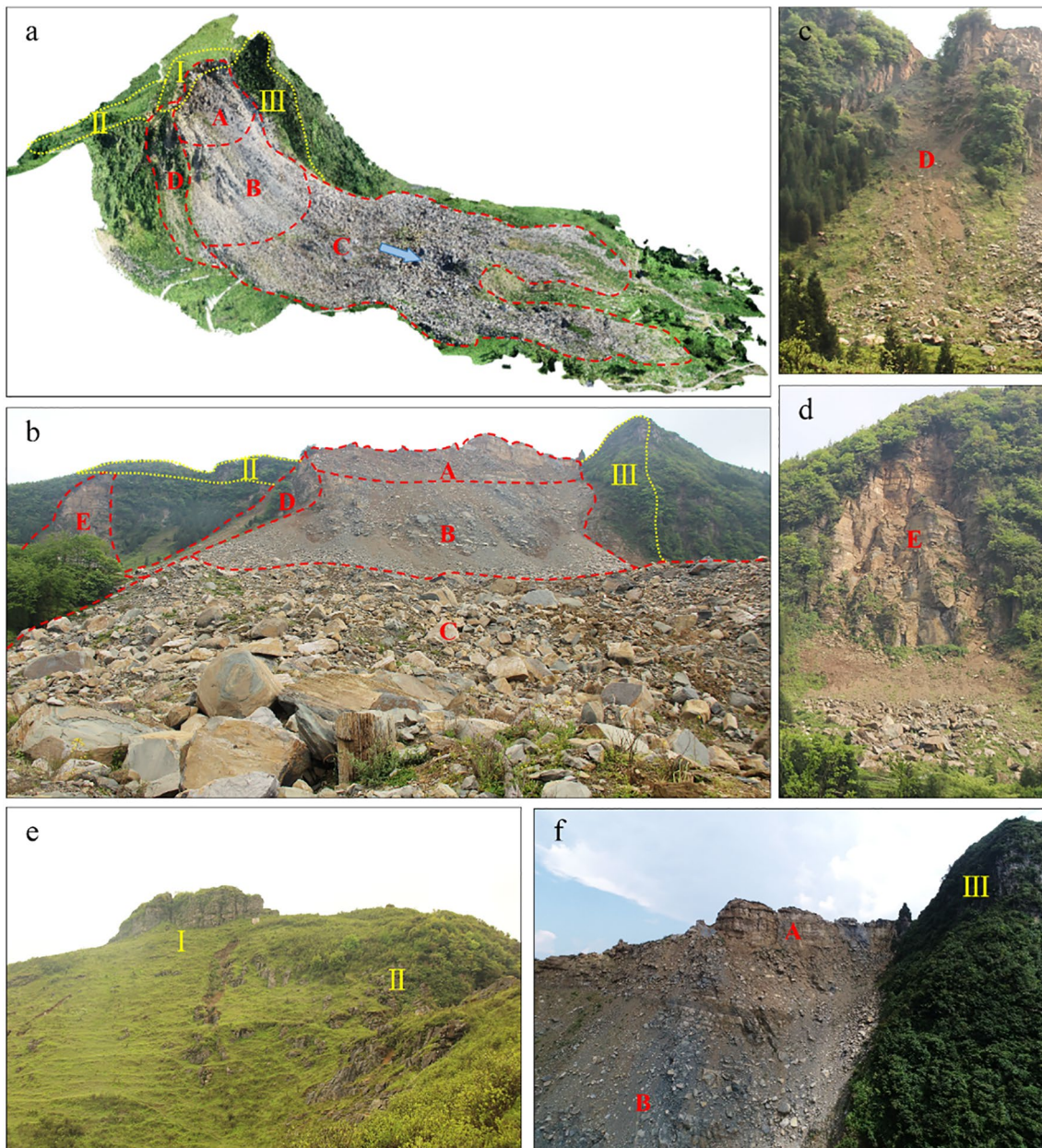
Fig. 4 Overview of the August 28, 2017, Pusa landslide: **a** UAV image (lateral view); **b** camera image (front view). Landslide-affected surrounding areas: **c** zone D; **d** history collapse (zone E); the unstable rock masses in the rear part (**e**) and on the south flank (**f**) of the source area. In (**a**) and (**b**), A–E mark the zones of major sliding; I–III are different areas affected by instabilities

20 m wide, with a strike angle of 235°. Field investigation noted that although several cracks developed in the rear of the slope, this zone seemed still well fixed with the bedrock. The possibility of overall failure of the rock mass in a short time is small, but the possibility of local rockfall cannot be ruled out.

After the landslide event, a series of tension cracks (strike angle 40°) were detected in the unstable rock mass on the south flank (zone III), the longest of which was about 50 m long, several meters wide and at least 4–5 m deep. The good

connectivity of cracks can greatly undermine the overall stability and will cause secondary disasters in case of rock mass instability.

3.2 Similitude Model Experiments

The model test took the Pusa landslide as the geological prototype, adopted similar material model test research method, and simplified the geological prototype according

to the actual geological conditions. The failure process under the mining effect was further studied using laboratory model experiments that simulated the gravitational deformation of slope models over a limited time span.

3.2.1 Determination of Similar Conditions

Referring to the research results of model test related to coal seam mining and overburden deformation (Zheng et al. 2015; Tao et al. 2020), and based on the theory of similarity triple theorem, it was ensured that the model and geological prototype meet the requirements of geo-mechanics similarity in geometry, kinematics and dynamics. The following parameters were considered in the modeling:

Geometric parameter: object size (L);

Time parameters: deformation time (t), and deformation velocity (v);

Physical and mechanical parameters: gravity acceleration (g), rock bulk density (γ), rock uniaxial compressive strength (R_c), elastic modulus (E), cohesion (c), and internal friction angle (φ). Among them, L, g and γ were the primary dimensions.

The similarity ratio formula of each parameter was listed, and the interrelationship between each parameter and the primary dimensions was derived according to the similarity criterion. In the formula, p represented the prototype parameter, m represented the model parameter, and C represented the similarity ratio, which was the ratio of the prototype parameter to the model parameter:

(1) Geometric similarity ratio: $C_L = L_p/L_m$
(2) Similarity ratio of gravity acceleration: $C_g = g_p/g_m$
(3) Similarity ratio of bulk density: $C_\gamma = \gamma_p/\gamma_m$
(4) Similarity ratio of deformation time:
$C_t = t_p/t_m = \sqrt{C_L/C_g}$
(5) Similar ratio of deformation velocity:
$C_v = v_p/v_m = \sqrt{C_L C_g}$
(6) Similarity ratio of compressive strength:
$C_{R_c} = R_{c \cdot p}/R_{c \cdot m} = C_L \cdot C_\gamma$
(7) Similarity ratio of elastic modulus:
$C_E = E_p/E_m = C_L \cdot C_\gamma$
(8) Cohesion similarity ratio: $C_c = c_p/c_m = C_L \cdot C_\gamma$
(9) Similarity ratio of internal friction angle:
$C_\varphi = \varphi_p/\varphi_m = 1$

After fully considering the size of the study area and the physical characteristics of the model materials, the geometric similarity ratio of the model was determined to be $C_L = 200$(simulating part of the slope with horizontal distance of 400–700 m and height of 1850–2150 m a.s.l in Fig. 2); the gravity acceleration similarity ratio was $C_g = 1$; the bulk density similarity ratio was $C_\gamma = 1.5$; the similarity

ratio of deformation time was about $C_t \approx 14$; the similar ratio of deformation velocity was about $C_v \approx 14$; the similarity ratio of compressive strength, elastic modulus and similarity ratio of cohesion were $C_{R_c} = C_E = C_c = 300$; the similarity ratio of internal friction angle was $C_\varphi = 1$.

3.2.2 Similar Materials and Test Proportion

Physical model similar materials were usually prepared from several materials in a certain proportion. According to the requirements of similarity and previous research experience (Chen et al. 2015; Du et al. 2021), it was determined that fine river sand (particle size of 0.25–0.35 mm) was used as aggregates in each rock strata, gypsum powder was used as cementitious material and water as solvent material. If the calculation was carried out according to the geometric similarity ratio formula, the thickness of the actual rock strata in the model was mostly less than 1 cm, and the thin and medium-thick rock strata were even less than 0.5 cm in the model. It was unrealistic to make all the mechanical parameters of the model completely similar to those of the actual slope. Therefore, when determining the proportion of similar materials through material ratio orthogonal experiments, the compressive strength was mainly similar, and the similarity of bulk density, elastic modulus and other indicators were fully taken into account. Since the initial setting time of gypsum was usually less than 10 min, which was not conducive to the pouring of slope model, so a little gypsum retarder was needed to delay the initial setting time. According to the pouring experience of the test model, it took about 20–30 min for similar materials to be mixed from the beginning to be filled on the model frame. After calculation, the proportion of gypsum retarder was finally determined to be about 0.15% of the gypsum weight in similar materials.

3.2.3 Model Design Scheme

The length, width and height of the laboratory model frame were 300, 30 and 200 cm, respectively. The steel plates on both sides and bottom of the model frame were used as boundary conditions to restrict the horizontal and vertical displacement of the model, and the upper part was a free surface. To embody typical geographical features (e.g., the broken block rock at the rear edge of the avalanche source area, deep and large karst fissures at the slope top and fault) in the test model, and ensure the operability of the model construction, the upper part of the slope was simulated by rock block stacking, and the position of karst fissures was reserved in the stacking process. The length, width and height of the rock block were 30, 3 and 4 cm, respectively, and no substance was

Table 1 Physical and mechanical parameters of rock strata and similar material

Parameters	Lithology					Similar materials	
	Limestone	Marl	Argillaceous siltstone	Silty mudstone	Coal seams	Targeted value	Actual value
Density (g/cm^3)	2720	2680	2650	2480	1400	1683	1580
Compressive strength (MPa)	75.6	92	102	68	20	0.23	0.24
Elastic modulus (KPa)	36,700	30,000	22,000	14,000	5400	46.7	39
Cohesion (KPa)	16,600	7500	11,500	5900	600	–	57
Internal friction angle (°)	41.5	32	34	30	26	–	31
Poisson's ratio	0.27	0.28	0.30	0.32	0.38	–	–

used to glue the rock blocks together during the stacking process. The coal seam roof was simplified as a homogeneous rock layer of silty mudstone, and similar materials were used for simulation. The final determination of the similar material bone glue ratio was 5.5:1. The detailed mechanical parameters of each stratum and similar material were demonstrated in Table 1. The thickness of single-layer similar material was about 2–4 cm, and mica powder was used to separate the layers between the strata (Ma et al. 2020). The fault was set at the toe of the slope, and its angle with the horizontal plane was 70°, which was used to simulate the fault F2 existing in the actual slope. Li et al. (2020) pointed out that the breakage of thick and hard intermediate strata has a decisive influence on the movement of overburden. However, the soft and thin intermediate strata will be deformed simultaneously with the overburden. The intermediate strata of M14 and M10 was silty mudstone with a thickness of 15 m, which

was in line with the characteristics of soft and thin intermediate strata. Therefore, an equivalent coal seam was set instead of M14 and M10 in the test, and the thickness was appropriately increased to 4 cm to provide sufficient movement space for the overburden deformation. Wet river sand was used to simulate the coal seam because it was easy to extract from the model. Since the coal seam floor had little effect on the stress and strain of the mining slope, the model floor was set as a rigid base and was poured with brick cement. The test model and micro-soil pressure sensor placement points were shown in Fig. 5.

Considering the influence of coal seam mining sequence on slope stability, two mining methods, i.e., descending mining (toward the inside of the slope) and ascending mining (toward the free surface), were adopted. Two models needed to be made, each model had four working faces, each working face length was 45 cm, from outside to inside working face number was X1, X2, X3,

Fig. 5 Test model and placement point of micro earth pressure sensor
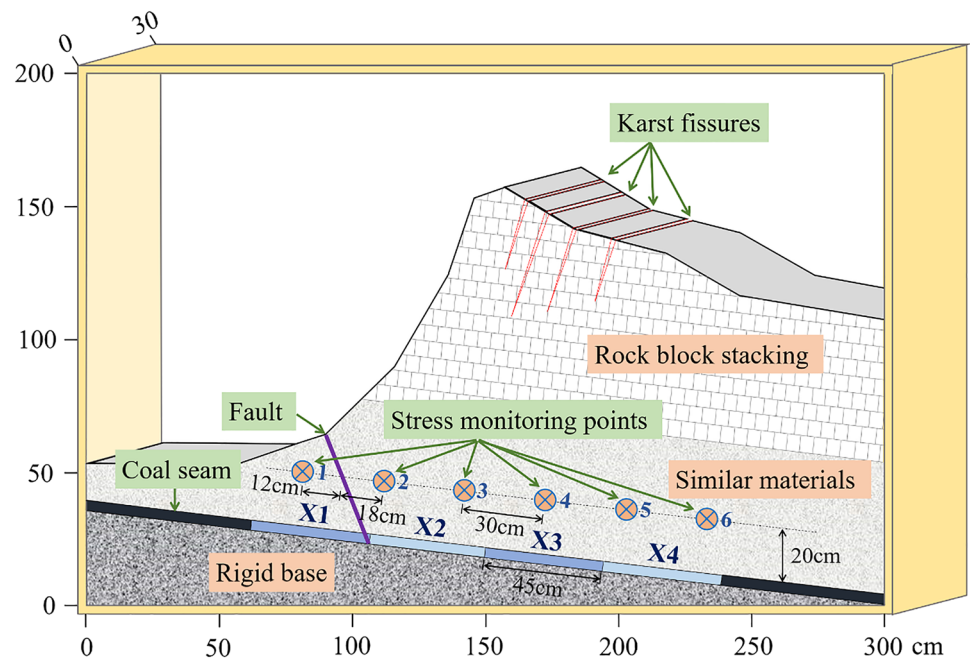
X4. Progressive excavation was carried out at the bottom of the model. The descending mining sequence was X1 → X2 → X3 → X4, and the ascending mining sequence was X4 → X3 → X2 → X1. The mining time of each working face was 15–20 min, and the physical simulation model balanced for 15–30 min after mining each interval.

3.2.4 Pressure and Displacement Monitoring

Six pressure monitoring points were arranged at 20 cm above the coal seam, with 30 cm spacing between adjacent monitoring points. The leftmost monitoring point was arranged in the footwall of the fault, with a distance of 12 cm from the fault surface (Fig. 5). The micro-soil pressure sensor was used for pressure monitoring, and its measurement range was 0–50 kPa with a resolution of no more than 0.05 FS. The pressure mentioned later refers to the overburden pressure on the surface of the soil pressure sensor, which is completely different from the concept of stress in the actual slope, especially in terms of numerical values. Therefore, it is of little significance to deduce the actual stress in the slope using monitoring point pressure through the similarity ratio formula, but the variation law of monitoring point pressure can still reflect the change of the actual stress in the slope to some extent. Before coal seam mining, the value of the sensor was zeroed out, so as to facilitate the observation of the change in pressure values for subsequent analysis. We consider that when the pressure is negative it indicates a decrease in pressure, and when the pressure is positive it indicates an increase in pressure.

This test displacement measurement applies XTDIC 3D full-field strain measurement system (XTDIC-CONST), which can quickly, efficiently and accurately obtain the three-dimensional coordinates, displacement and strain data of the model in the process of deformation (Zhou et al. 2021). The system integrates Digital Image Correlation (DIC) and Binocular Stereo Vision. By tracking the speckle images of the object surface in each deformation stage in real time, and using image correlation algorithms for stereo matching of the deformation points, the three-dimensional spatial coordinates of the matching points are reconstructed. The displacement field data are smoothed and the deformation information is visualized analysis to realize real-time calculation and output of non-contact 3D deformation measurement. The system consists of high-resolution digital single-lens reflex (SLR) camera, stress–strain analysis system, supplementary light, data transmission line and computer. It has been widely used in material research, structural analysis, part measurement, aerospace and other fields.

3.2.5 Model Making Steps

The steps of model making are as follows:

1. Number the templates in order from bottom to top and install them on the model frame. After drawing the model boundary line on the inside of the templates, remove the templates from top to bottom one by one, and retain the bottom few pieces of the template for pouring the rigid base.
2. Prepare of similar materials according to test proportion.
3. Spread a layer of wet river sand about 4 cm thick evenly on the rigid base first, and then fill a layer of similar material about 2–4 cm thick, and a layer of mica powder about 2–3 mm thick, respectively.
4. Repeat step 3 and properly bury the micro-soil pressure sensor in predetermined position until the lower half of the model is completed.
5. To simulate the existence of deep and large karst fissures at the top of the slope, the iron plate with customized size should be embed in a "V-shaped" manner at the predetermined position in the process of rock block stacking. When the model is completed, the iron plate is extracted and filled in the fissures with river sand (Fig. 6a).
6. The finished model is first left to rest for 1 day, and the model surface is coated with white paint for smooth treatment (Fig. 6b). After the model is set for another

Fig. 6 Model making steps 5 and 6: **a** model production completed; **b** apply white paint on the model surface for smooth treatment; **c** Scattered spots are painted on the model surface randomly
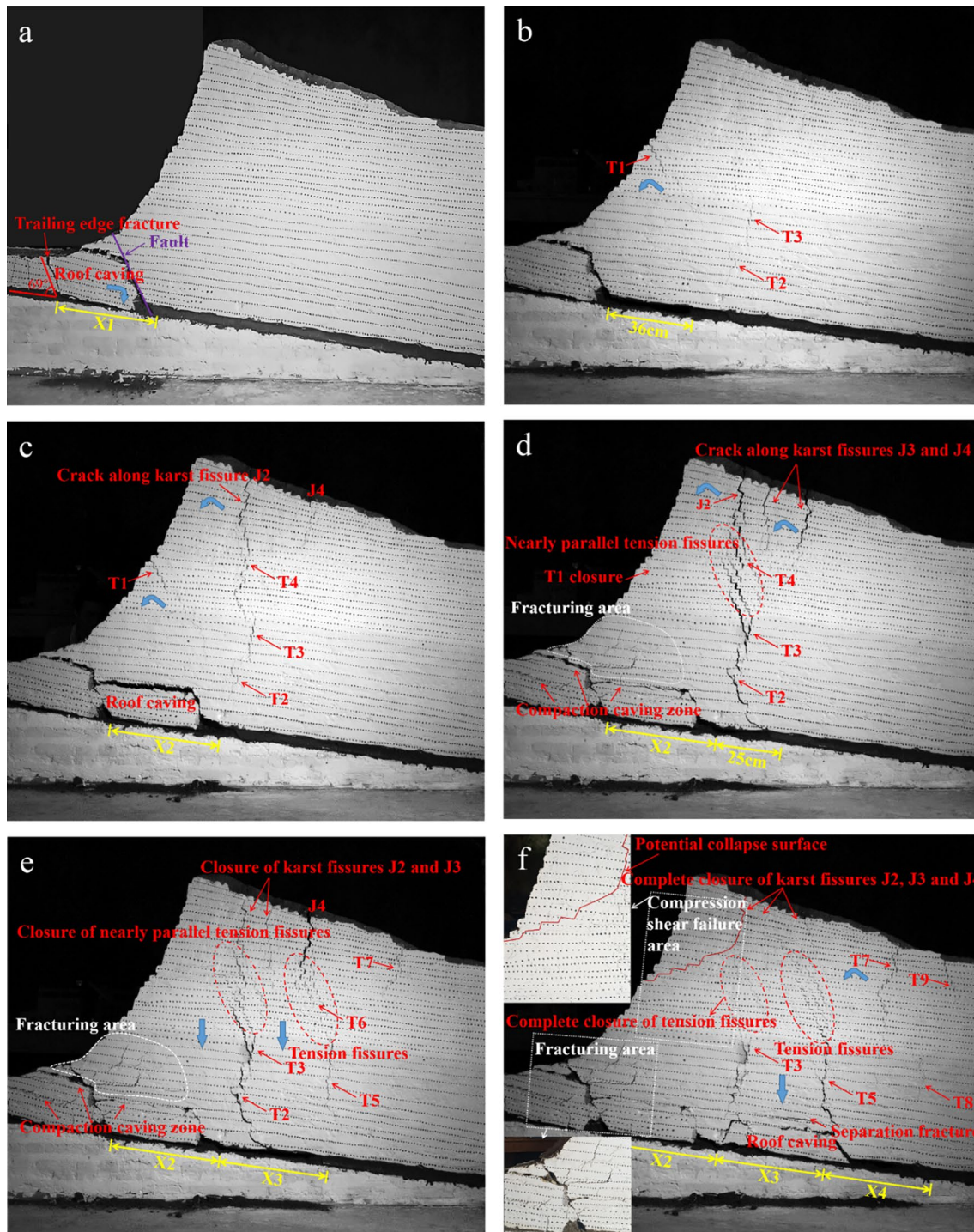
Fig. 7 Overburden movement and fracture evolution during descending mining: **a** excavation of X1; **b** excavation to X1 + 36 cm; **c** excavation of X2; **d** excavation to X2 + 25 cm; **e** excavation of X3; **f** excavation of X4. Since the photographs taken by the camera are oblique views, which affects the scale and relative proportions of the object, the measured lengths and angles are annotated. The direction of the blue arrow in the figure indicates the deformation direction of the overburden

day, a fine brush is used to dip in black paint to paint scattered spots randomly along the direction parallel to the coal seam on the model surface, with the spacing of scattered spots about 1–2 cm (Fig. 6c). The model con-

tinues to be maintained at room temperature for 4 days after removal of the template.

4 Model Experiments Results

4.1 Slope Deformation Process in Descending Mining

4.1.1 Overburden Movement and Fracture Evolution

In the test, the whole process was photographed with a high-resolution digital SLR camera and the overburden movement and fracture evolution of the pillar-less mining can be clearly seen (Fig. 7).

4.1.1.1 Mining Working Face X1 After the mining of working face X1, the rock stress gradually shifted to the coal wall near the working face, and the hanging arch span of the immediate roof increased. The deformation state of the roof can be compared to the bending deformation at both ends of the fixed end (Liao et al. 2020). When working face X1 was fully mined to the bottom of the fault, the roof was rotated and sunk to the side of the goaf under the shear stress. Trailing edge fracture developed to the top rear 69° of the goaf. At this point, the deformation state of the roof can be analogized to the cantilever beam tension fracture with the left unexcavated rock as the fixed end and the right fault footwall as the free end, which conforms to the cantilever beam hypothesis proposed by Unrug and Szwilski (1982) (Fig. 7a).

4.1.1.2 Mining Working Face X2 After excavation of 36 cm, a diagonal downward developing tension crack T1 with an angle of about 56° appeared on the slope surface. Two vertical tension cracks T2 and T3, with a total length of about 45 cm, also appeared in the middle of the slope, developing downward to the roof. The overburden underwent the first tension fracture toward the free surface, and after rotating and sinking, it formed support with the roof falling from the footwall of the fault in contact with each other. The analysis suggests that after the underground coal seam is mined out, the pressure balance arch is formed in a certain range above the goaf (Kratcsch 1986). The rock strata in the pressure balance arch lose support and are in the state of unloading. Under the action of self-weight stress and the vertical pressure of the overburden, the bending subsidence of the rock strata occurs, and fracture and collapse occur after reaching the bending limit (Fig. 7b)).

When a 90 cm (X2) length was excavated, the immediate roof partially collapsed with a caving height of 9 cm and a complete shape, which is known as the initial collapse. The rock mass in the upper part of the caving roof continued to rotate and sink due to the loss of the lower support, resulting in the crack T1 being pulled apart. The rock mass

above the right side of the crack T1 was in a cantilever bending state, and the slope body undergone the second tension fracture. The deep and large karst fissure J2 was connected with cracks T4, T3 and T2 to form fracture boundary. It can be seen that the existence of deep and large karst fissure provides an advantageous channel for the development of tension cracks (Fig. 7c).

4.1.1.3 Mining Working Face X3 After the excavation of 25 cm, the slope occurred severe integral dumping subsidence under the action of self-weight stress, resulting in the closure of crack T1, and the caving zone was violently squeezed. Numerous cracks appeared at the slope toe, forming a fracturing zone. Several tension cracks with nearly parallel distribution appeared near the crack T4, and the crack T2 developed to the lower right extending into the goaf. The deep and large karst fissures J3 and J4 also opened and expanded downward due to the continuous deformation of the slope. The accumulation and arrangement of rock strata directly affect the morphology of tension cracks. In the lower part of the model filled with similar materials, the tension cracks on the slope surface are mostly distributed in vertical strip. In the upper part of the model made by the block stacking, several nearly parallel stepped tension cracks are developed along the block gaps (Fig. 7d).

When excavated to the middle of the slope (X3), the overburden showed a trend of integral subsidence to the center of the coal seam. Constrained by deep and large karst fissures, fissures J2 and J4 extended downward to become fracture boundaries, and the slope was obviously divided into three deformation blocks with the reference of mining working face X2, X3 and X4. However, the damage degree and deformation rate of the three blocks were different. As working face advanced, the slope blocks deformed successively and gradually reached a new stable state. The tension cracks J2, J3 and T4 at the rear of working face experienced a dynamic process from open to close (Wang et al. 2015). It can be seen that with the gradual mining of coal seam, the deformation trend of the slope changes from rotary dumping to vertical subsidence, and the surface subsidence changes from non-sufficient mining subsidence state to full mining subsidence state (Fig. 7e).

4.1.1.4 Mining Working Face X4 During the excavation of working face X4, the immediate roof was abscised again, showing a weak bending, and a separation fracture appeared above. The middle block of the slope lost the lower support and undergone significant settlement. The rightmost block of the slope was in the state of cantilever bending stress and tilted toward the free surface side, resulting in the appearance of tension cracks T7, T8 and T9 above and in front of the working face X4. Tension cracks and karst fissures (T1, T4, J2, J3, J4) originally developed on the slope at the rear of
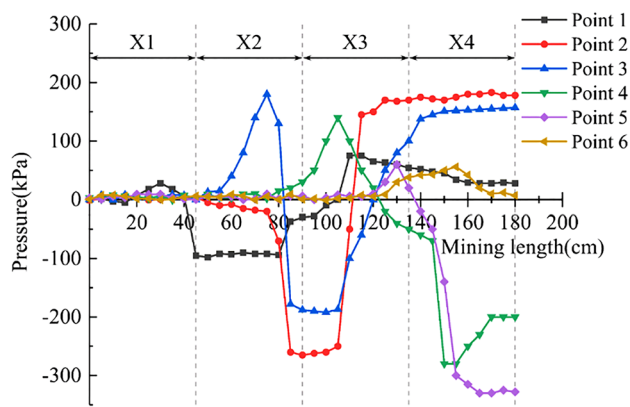
Fig. 8 Variation of overburden pressure in descending mining

the working face were completely closed. The three phases of undeveloped, developing, full compaction of cracks are the dynamic process of the gradual transfer of goaf space to the ground surface. In the process of settlement, the slope will also be subjected to shear failure due to the effect of gravity component. Careful observation of the middle and upper slope surface can reveal that numerous small cracks are visible to the naked eye in the area. Analysis suggests that these cracks should be compression–shear cracks, and the area is a compression–shear stress concentration zone. The compression–shear cracks and karst fissure J2 are interconnected to form the potential collapse surface of the slope. Once the rock mass at the shear outlet is deformed and destroyed, the rock mass at the top of the slope will collapse outward as a whole (Fig. 7f).

4.1.2 Variation Law of Overburden Pressure

The pressure change curves of each monitoring point of coal seam roof during the test are shown in Fig. 8. In the figure, the abscissa is working face advancing distance, the longitudinal coordinate is the pressure. With the beginning of coal seam mining in X1, the pressure at monitoring point 1 in the footwall of the fault increases slightly under the influence of leading abutment pressure. When the mining of working face X1 is completed, the roof of coal seam rotates clockwise and sinks, and the pressure at monitoring point 1 decreases rapidly, but the pressure at other monitoring points remains basically unchanged. As mining continues, the pressure at monitoring point 2 does not increase, but slowly decreases, due to the fault effectively blocking the transmission of leading abutment pressure in the slope. Affected by leading abutment pressure, the pressure at monitoring point 3 gradually increases and the pressure peak appears. Mining X1 + 36 cm to X2 section of working face, the pressure at monitoring points 2 and 3 decreases significantly. Monitoring point 1 is squeezed by the rock mass in the hanging

wall of the fault, and the pressure starts to increase. The pressure at monitoring point 4, located ahead of the working face advance, is also slowly increasing. At this time, the slope is undergoing the first and second cantilever fracture failure and the first large-area collapse of the roof. Mining X2 to X2 + 15 cm section of working face, the pressure at monitoring points 2 and 3 changes very little, and the pressure at monitoring points 4 and 1 gradually increases to the local peak. Subsequently, the pressure at monitoring points 2 and 3 increases rapidly, the pressure t monitoring point 4 decreases gradually, and the pressure at monitoring point 5 increases first and then decreases. This is precisely caused by the severe integral dumping subsidence of the slope that the caving zone is strongly squeezed. Thereafter, monitoring points 2 and 3 are always in a high stress concentration state. The pressure at monitoring point 1 decreases because the rock mass under the fault is compressed and cracks appear, releasing part of the pressure. Mining X3 + 10 cm to X3 + 20 cm section of working face, the pressure at monitoring points 4 and 5 decreases rapidly, which indicates that coal seam roof collapses once again in a large area. The rock mass without lower support will continue to settle and compact the caving zone, resulting in an increase in the pressure at monitoring point 4. The pressure at monitoring point 6, which is located at the boundary of working face, first increases and then decreases. The reason for the increase of pressure is due to the influence of leading abutment pressure.

With the transfer and rebalance of stress, the overburden deformation process has obvious periodicity, which is a complete cycle from stress concentration, damage deformation, fracture and collapse, stress release. Precisely because of this internal mechanism, the variation law of strain measured by soil pressure sensor is reliable to reflect the internal stress evolution process of mining rock mass. The pressure at all monitoring points and the deformation of overburden sequentially experiences the change process of increasing (leading abutment pressure action), substantial reducing (roof separation or collapse), slightly increasing (crack generation and expansion), substantial increasing (integral slope subsidence) and maintaining stability (new stable state of rock mass structure). The average mining distance interval corresponding to the peak pressure affected by the leading abutment pressure at each monitoring point is 25 cm. It can be seen that there is tension–compression stress transformation in the rock mass ahead of the advancing direction of working face. However, the variation range of pressure curves of each monitoring point is different, among which the pressure at monitoring points 2 and 3 are the largest, indicating that the pressure concentration at the toe of the slope is obviously better than that at other parts of the slope (Lin et al. 2018).
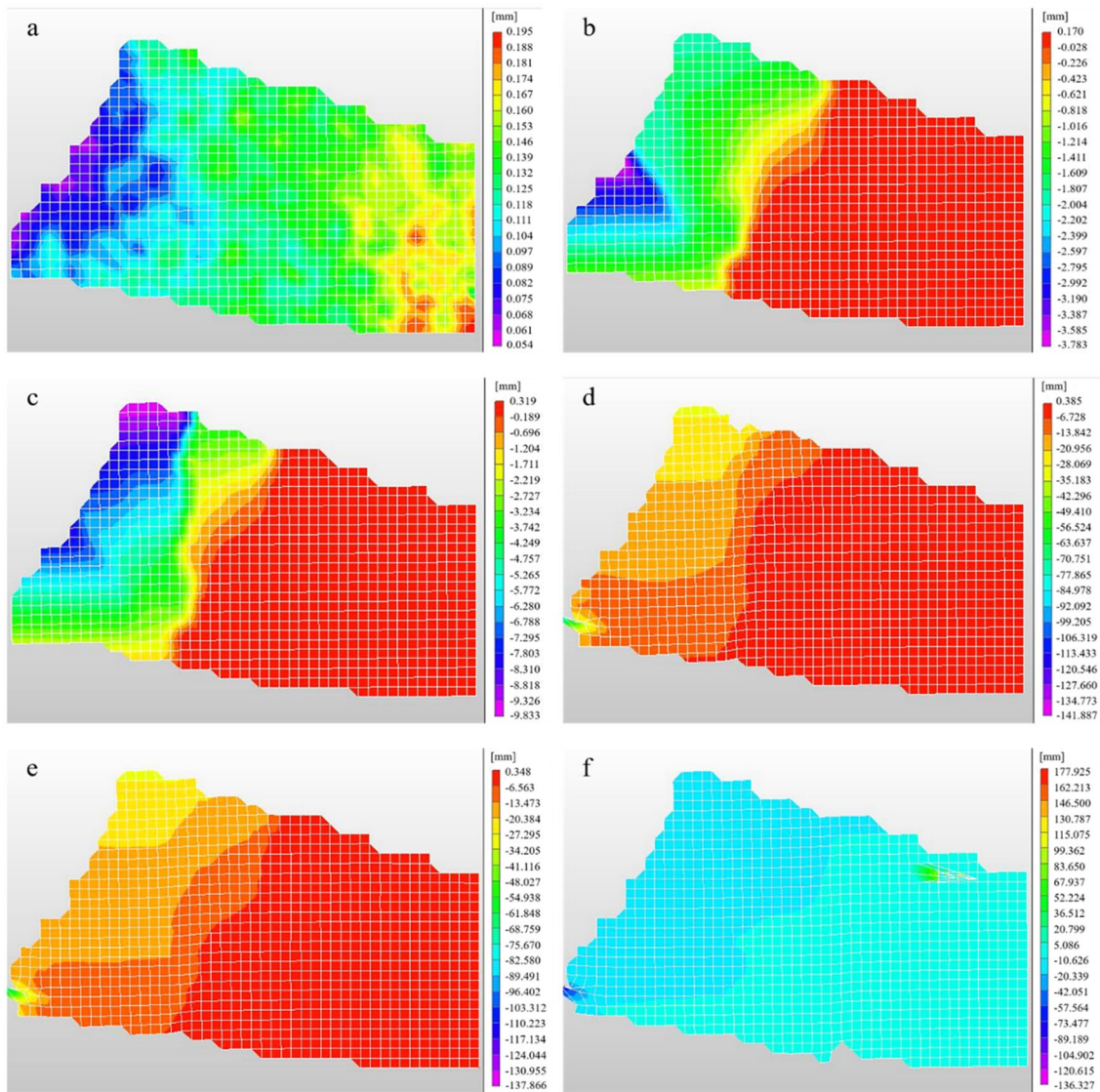
Fig. 9 Horizontal displacement nephograms of overburden in descending mining: **a** excavation of X1; **b** excavation to X1 + 36 cm; **c** excavation of X2; **d** excavation to X2 + 25 cm; **e** excavation of X3; **f** excavation of X4

4.1.3 Variation Law of Overburden Displacement

Photographs of the deformation process of the model are processed to obtain the horizontal and vertical displacement nephograms of the overburden during the descending mining, as shown in Fig. 9 and Fig. 10, respectively. In the horizontal displacement nephogram, the positive value indicates movement toward the inside the slope and the negative value indicates movement toward the free surface. In the vertical displacement nephogram, the positive value indicates downward movement and the negative value indicates upward movement. It should be noted that since the measurement system is suitable for measuring continuous displacement changes, the areas with severe deformation in the model, such as the caving zone or tension crack concentrated area, may be missing. In the displacement nephograms of Figs. 9d–f, 10d–f, the areas of equipotential lines mutation are the areas where deformation data are missing. After using the difference-completion hole method to fill in the missing areas in the displacement nephograms, it is found that the failure characteristics of continuous deformation presented differ from those of the actual discontinuous deformation, and the displacement values are often too large and do not have statistical significance. Since the image can still reflect the overall deformation law of the slope, this subsection only analyzes the displacement variation characteristics of the overburden above the caving zone.
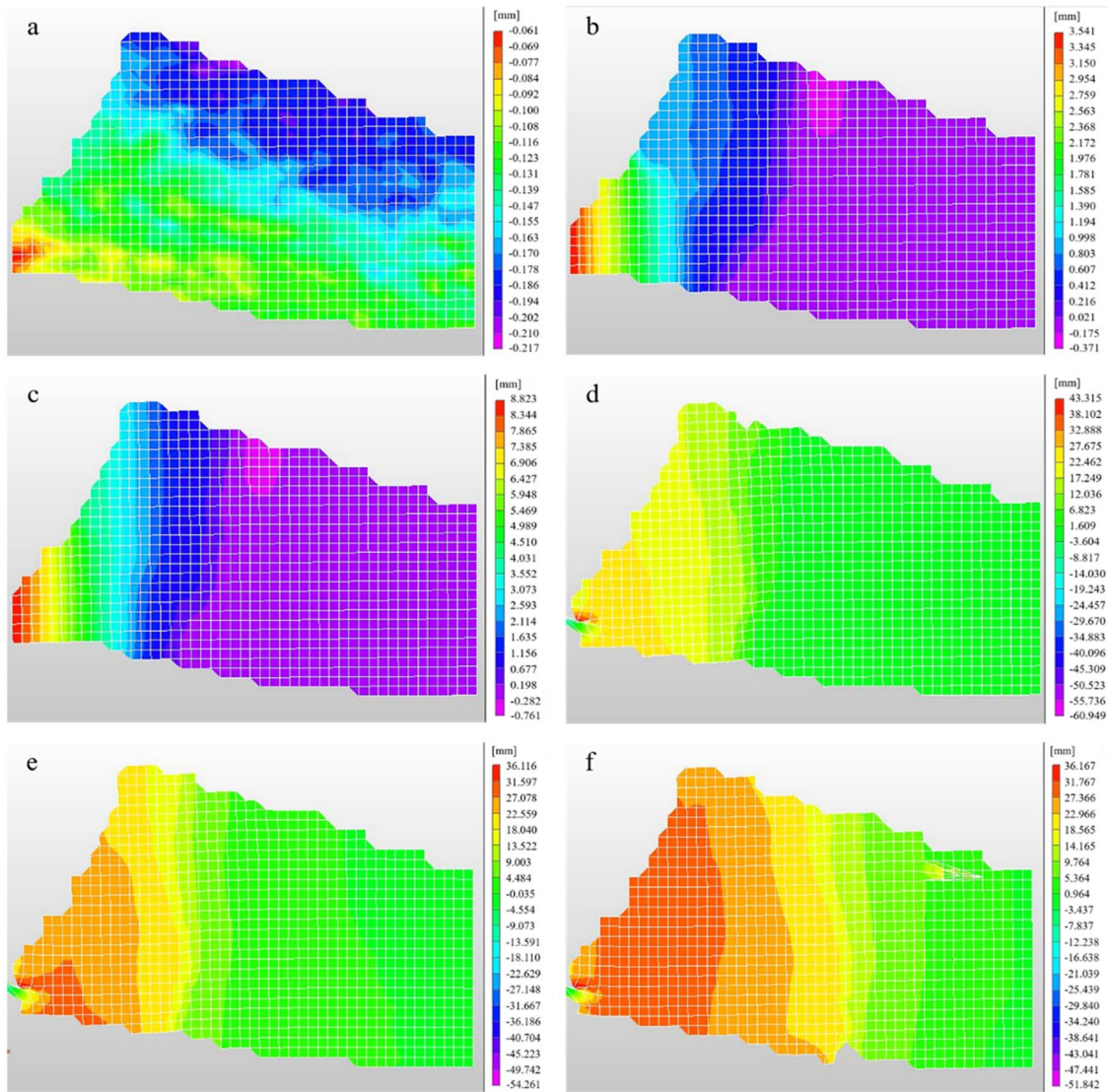
Fig. 10 Vertical displacement nephograms of overburden in descending mining: **a** excavation of X1; **b** excavation to X1 + 36 cm; **c** excavation of X2; **d** excavation to X2 + 25 cm; **e** excavation of X3; **f** excavation of X4

The displacement monitoring results show that after the excavation of working face X1, the horizontal and vertical displacement of the overburden are almost zero, which shows that the fault can block the influence of the rock mass collapse on the overburden. When mining to the X1 + 36 cm, the overburden is in the cantilever bending limit state, and the first tension fracture toward the free surface occurs. The maximum horizontal displacement in the middle of the slope surface is −3.783 mm, which is twice the horizontal displacement at the top of the slope. The maximum vertical displacement at the outermost end of the overburden cantilever is 3.541 mm. During the process of mining working face X2, the first large area caving of coal seam roof occurs, with the caving length of about 38 cm, and the second tension fracture of the slope occurs. The maximum horizontal

displacement of the top of the slope is −9.833 mm, and the horizontal displacement of the middle and upper part of the slope is significantly increased. The vertical displacement at the outermost end of the overburden cantilever is still the largest, reaching 8.823 mm. The deformation direction of the overburden is exactly the same as that of the blue arrow in Fig. 7. With the successive mining of working face X3 and X4, coal seam roof collapses periodically, and the mining influence range expands to the deep part of the slope. From the horizontal displacement nephogram, it is not difficult to see that the equipotential lines penetrate diagonally downward from the top of the slope to the free surface, and its shape is similar to the arc. Based on the distribution of equipotential lines, it can be inferred that with the intensification of deformation, the overburden may occur tensile–shear–slip

instability, especially the rock mass around the top of the slope has the greatest possibility of instability. The morphology of the equipotential lines in the vertical displacement nephogram is similar to that of the fracture boundary formed by the interconnection of karst fissure and tension fractures in Fig. 7. The overburden above the unmined coal seam is basically not deformed.

To further explore the temporal and spatial variation of overburden movement during the mining process, typical monitoring lines and data points are extracted from the displacement nephograms for analysis. Three transverse displacement monitoring lines, numbered A, B and C, are selected from bottom to top along the direction parallel to the coal seam. Line A is located in the lower part of the slope filled with similar materials, line B and line C are located in the upper part of the slope built with rock blocks. A speckle is selected as the data point at a certain interval on the monitoring line, and a total of twelve columns of the data points are divided. Taking working face as the boundary, the data points in 1st columns to 4th column are above working face X2, 5th column to 7th column are above working face X3, 8th column to 10th column are above working face X4, and 11th column and 12th column are above the unmined coal seam (Fig. 11). The horizontal displacement and vertical displacement of all data points are counted, and the displacement variation laws of transverse monitoring lines during descending mining are obtained, as shown in Fig. 12. The meanings of positive and negative values of displacement in the figures are the same as those in the displacement nephograms.

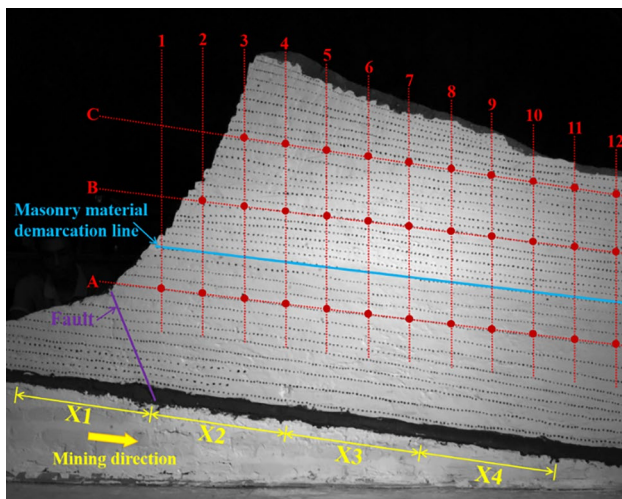In the process of mining to X1 + 22 cm, the changes of horizontal and vertical displacements of the three monitoring lines are very small and negligible. Mining X1 + 22 cm to X2 section of working face, the rock mass near the slope surface occur the first and second cantilever fracture failure, resulting in the deformation of data points A1–A4 on line A, B2–B5 on line B, and C3–C6 on line C. Continuing to mine working face X3, the slope undergoes the severe integral dumping subsidence, data points A5–A7 on line A, B6–B8 on line B, and C7–C9 on line C have deformation. At this time, the horizontal and vertical displacements of data points A1–A4, B2–B5 and C3–C6 increase significantly, and individual data points even show the maximum horizontal displacement. During the mining of working face X4, coal seam roof once again collapses in a large area and the slope body is significantly subsided. Data points A8–A12 on line A, B9–B12 on line B and C10–C12 on line C occur deformation. The horizontal and vertical displacements of data points A5–A7, B5–B8, and C5–C9 continue to increase, with the change rate of vertical displacement significantly greater than that of horizontal displacement. In contrast, the increase rate of vertical displacements of A1–A4, B2–B4 and C3–C4 slow down, and the horizontal displacement decrease instead. It can be seen that underground mining is bound to break the incipient stress equilibrium state of the slope, the deformation of the slope body occurs gradually with the gradual mining of the coal seam, and the influence range of mining is distributed in an inverted trapezoid within the overburden. On the whole, the horizontal and vertical displacements of the three monitoring lines during mining process gradually decrease along the descending mining direction, and the horizontal displacements of each column of data points from bottom to top gradually increase and the vertical displacements gradually decrease. However, when working faces X3 and X4 are mined, the vertical displacements of data points A1 and B2 are smaller than those of A2 and B3 and gradually tend to stabilize. It indicates that the rock mass that has been deformed and destroyed will gradually reach a new stable state.

4.2 Slope Deformation Process in Ascending Mining

4.2.1 Overburden Movement and Fracture Evolution

4.2.1.1 Mining Working Face X3 and X4
Face began to mine forward from the open-off cut. When working face in the model retreated 45 cm (X4), coal seam roof was slightly bent and deformed downward, but did not separate and collapse. When working face advances to working face X3 (90 cm), the immediate roof breaks for the first time, which is judged as the initial weighting of working face. The collapse height was 8 cm, the empty roof range was 75 cm, and the separation fracture was developed on the roof above the goaf (Fig. 13a). The force mode of the roof was similar to the beam bending structure fixed at both ends (Liao et al.
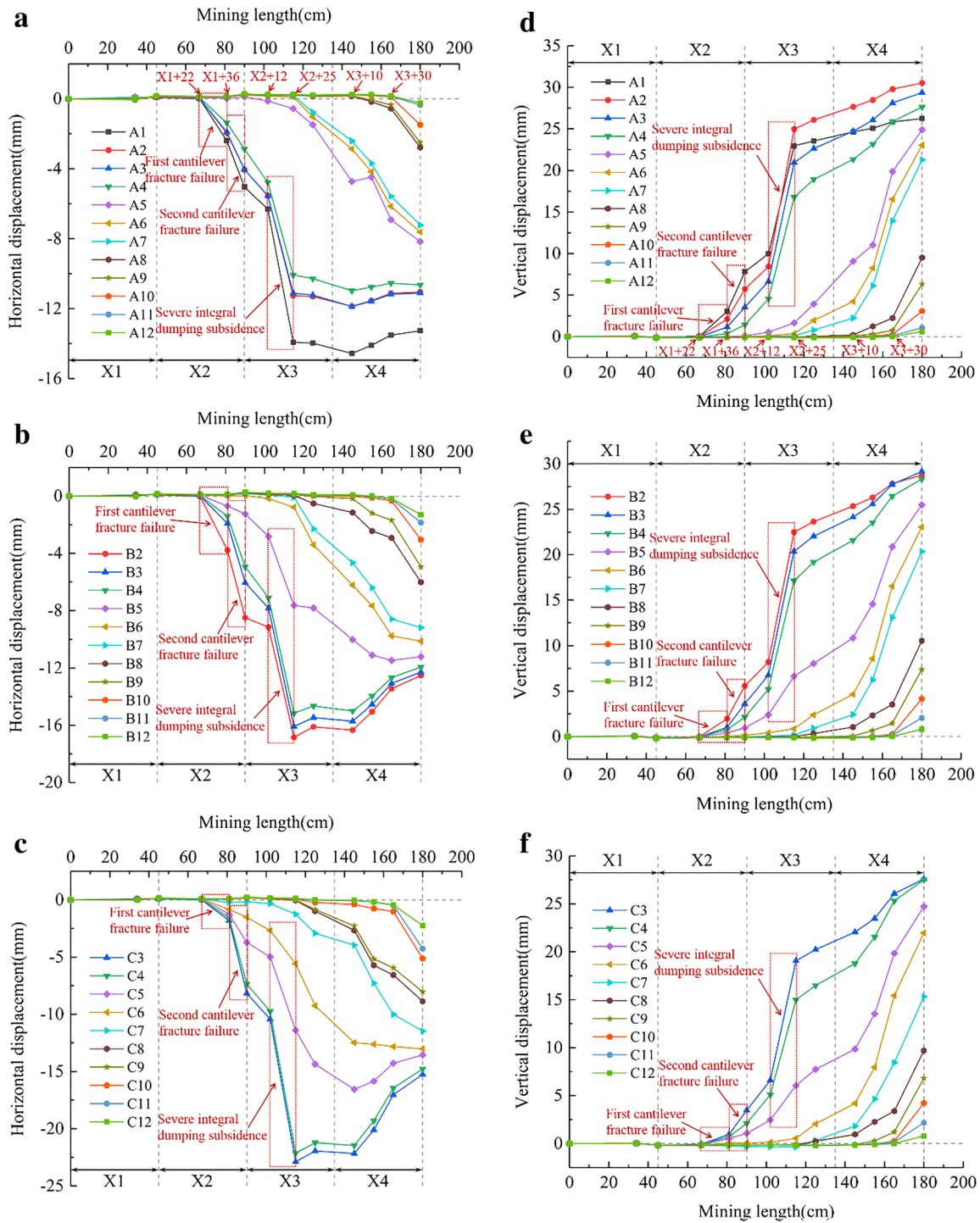

Fig. 11 Location of displacement monitoring lines and data points on overburden in descending mining

Fig. 12 Displacement variation curves of transverse monitoring lines in descending mining: **a** horizontal displacement of line A; **b** horizontal displacement of line B; **c** horizontal displacement of line C; **d** vertical displacement of line A; **e** vertical displacement of line B; **f** vertical displacement of line C

2020). During the continuous advancement of working face, the deformation of the roof is gradually transformed from elastic to plastic deformation, which does not cause the layer to break rapidly, but it will be suspended above the goaf and bears the weight of the overburden. When the elasto-plastic boundary line intersects, the two ends become plas-
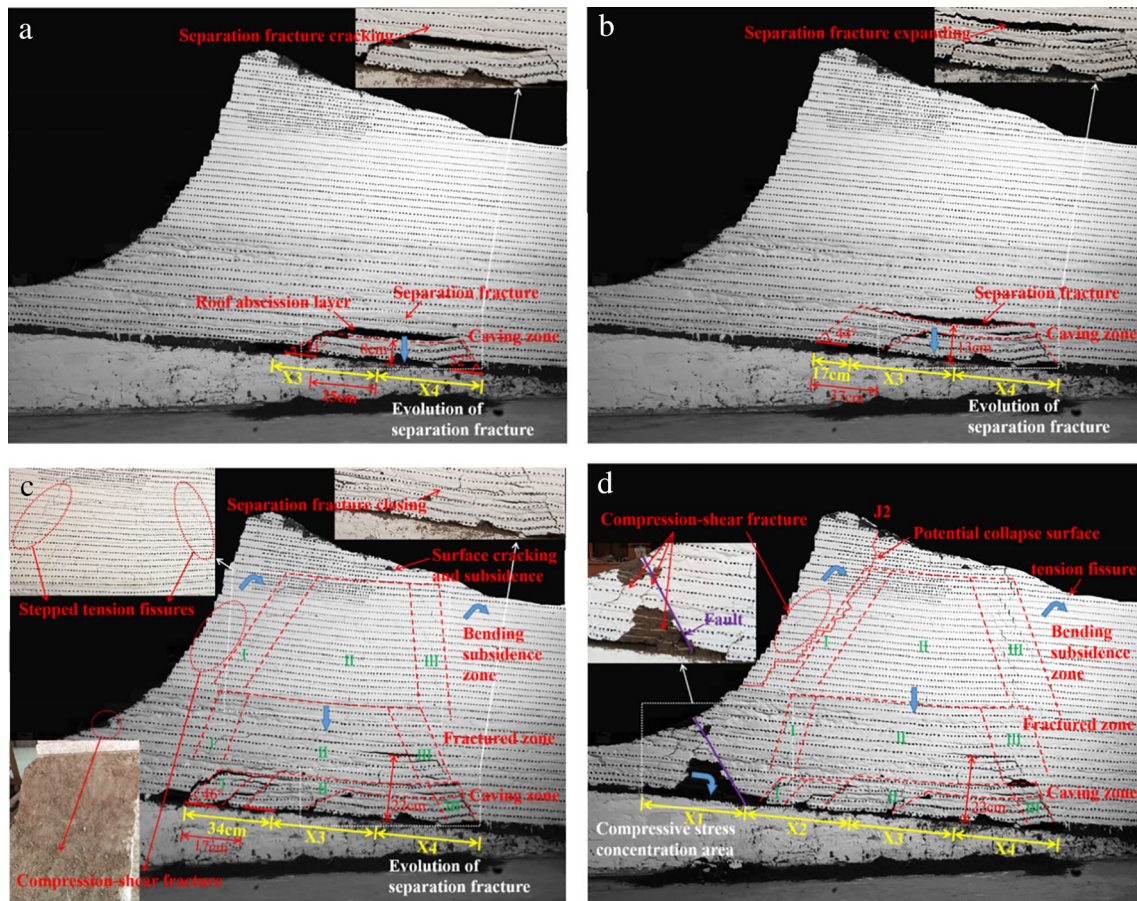
Fig. 13 Overburden movement and fracture evolution during ascending mining: **a** excavation of X3 and X4; **b** excavation to X3 + 17 cm; **c** excavation to X3 + 34 cm; **d** excavation of X4. Since the photographs taken by the camera are oblique views, which affects the scale and relative proportions of the object, the measured lengths and angles are annotated. The direction of the blue arrow in the figure indicates the deformation direction of the overburden

tic hinges, thus completely eliminating the bearing capacity and causing breaking. However, after the end of the elastic stage enters the plastic stage, the plastic states of the two ends are different. The "cantilever" fracture zone of the rock stratum on the open-cut side is shaped like a fan, which is a stable fracture development zone. The open-off cut side in a relatively stable state forms a plastic hinge first and fractures first, which is the fracture initiation and development zone (Yu et al. 2020). Due to the continuous stopping and starting of the mining process, cracks are still in the process of initiation and development (Xue et al. 2015). The angle between the fracture boundary and the coal seam is called the caving angle. Under the influence of rock strata tilt, the self-weight stress direction of the slope inclines to the right, and the subsidence center of the slope deviates to the left of the goaf center, so the caving angle of the right side (52°) is obviously larger than that of the left side (31°). In the process of mining working face X4 and X3, the influence of goaf on the slope does not reach the surface, and the overall deformation of the slope is small (Fig. 13a).

In the process of coal seam mining, the deformation degree of bending subsidence in each rock stratum varies greatly due to the different tensile stress of that. Tensile stress is generated horizontally between adjacent rock strata, and compressive stress is generated vertically. Inclined joints may change the principal stress from vertical and horizontal stress to sub-vertical and sub-horizontal stress. When the tensile stress on the face of the rock formation is greater than its tensile strength, and there is enough movement space in the lower part of the uncollapsed rock stratum, the separation fractures begin to expand in both horizontal and vertical directions (Fig. 13a, b). After the separation fractures get fully developed, some rock strata bend, fracture and collapse again, occupying the space of separated strata. With the closure of the original separation strata, the new separation strata begin to develop, and the separation space appears periodic disappearance and development (Fig. 13c). The alternate appearance of the separation space can also be regarded as the upward and forward transmission of goaf clearance

space in the overburden, and finally it is transmitted to the surface to cause surface cracking and subsidence. The evolution of separation fractures shows obvious synergistic effect, which is in accordance with the development law of cracking, expanding and closing (Fig. 13a–c).

4.2.1.2 Mining Working Face X2 As the working face advanced, coal seam roof occurred periodic collapse, and the overburden was trapezoidal damaged. When mining to working face X3 + 34 cm, the overburden undergone the first integral bending subsidence (Fig. 13c). Liu (1995) put forward the general understanding of "three horizontal zones" and "three vertical zones" for the division of failure zones of overburden. It is generally recognized that overburden in longwall extraction are divided from bottom to top into three different zones: caving zone, fractured zone and bending subsidence zone. Overburden are divided from left to right into three zones: stopping line fracture development zone (I), fracture compaction zone (II) and open-off cut fracture development zone (III) (Palchik 2005, 2015; Tao et al. 2015; Zhang et al. 2018a). When working face advances to working face X2 (135 cm), the maximum height of the caving zone was 13 cm, which was 3.25 times of the seam mining height. The roof strata were broken into irregular blocks and fell disorderly on the bottom plate. The maximum height of the fractured zone and the bending subsidence zone were 27 and 45 cm, respectively, which were 6.75 times and 11.25 times of the mining seam height. Periodic roof caving interval is called periodic weighting step (Lu et al. 2010). After measurement, the two weighting steps were 37 and 17 cm, and height of separation layer rose to 13 and 22 cm, respectively (Fig. 13b, c).

The "key stratum" mentioned in traditional strata control theory refers to a thick and hard group of stratum which play a major role in controlling the movement of mining overburden mass (Du et al. 2021). There is also the "key stratum" in the rock stratum with the same lithology, which controls the synchronous and coordinated deformation of the upper strata, and also weakens the upward transfer of the space of separated strata. Multi key stratum refers to that two or more groups of hard rock layers in the bedrock. One group of hard rock layer near the coal seam named "sub key strata" controls the local strata movement, and another group of hard strata named "main key strata" controls the deformation and movement of the whole overlying strata and even ground surface (Chen et al. 2019). Because the hardness of the rock block is larger, the bottom rock block stacking layer can be regarded as the main key stratum. The lowermost rock stratum in fractured zone is the sub key stratum. It can be seen that the bottom-up crushing degree of the slope is gradually reduced, the bending deformation degree of the rock stratum is gentle, and the integrity of the rock mass is enhanced.

Fractured zone and bending subsidence zone contain two forms of fissures, one is inclined fissures running through part of the rock layer with short length, mostly distributed in the fracture development area on both sides of the rock stratum and the area with large bending deflection in the middle of the rock stratum. Stepped tension fissures are obvious in the fracture development area on both sides of the bending subsidence zone. Another kind is the separation fracture between adjacent rock stratum, which is long in length and wide in width, mainly distributed in the fracture compaction zone in the middle of the rock stratum, and is the main influencing factor leading to the separation, fracture and collapse of rock stratum (Wu et al. 2018; Ning et al. 2019). The separation fractures developed 5–22 cm above the mined seam, which was 1.25–5.5 times of the seam mining height. The analysis of the mechanical characteristics of the slope deformation confirms that the fissure at the toe of the slope is a compression–shear fracture, indicating that the toe of the slope is a concentrated area of compression–shear stress, and the slope body has obvious shear subsidence along the fault (Fig. 13c).

4.2.1.3 Mining Working Face X1 In the mining process of working face X1, the slope body above the goaf has undergone the second integral bending subsidence, and the stepped tension fissures gradually developed from within the slope to the surface. The broken rock strata in the caving zone were compacted more tightly, and the separation fractures were also compressed significantly. The roadway in the physical model was completely destroyed with small residual space and poor stability. The rock stratum above the unmined coal seam behind the open-off cut showed a deformation tendency to dip toward the center of the slope, and tension cracks appeared at the back edge of the slope top (Fig. 13d). Many fine compression–shear cracks appeared in the area near the slope surface, the rock mass above the fault was deformed and bulged by squeezing, and coal seam roof below the fault was fractured and collapsed. The com-
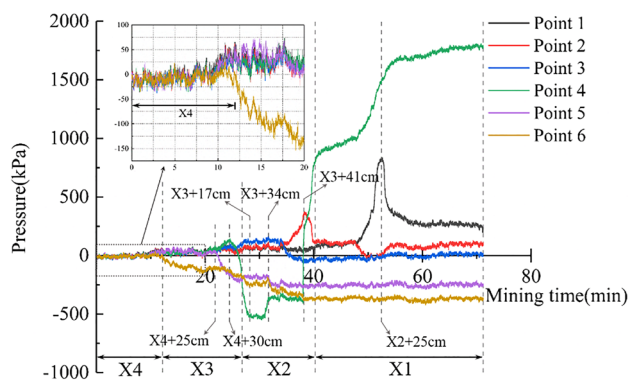

Fig. 14 Variation of overburden pressure in ascending mining

pression–shear cracks were interconnected with the tension cracks and karst fissure J2 to become a potential collapse surface, which seriously affected the stability of the slope (Fig. 13d).

4.2.2 Variation Law of Overburden Pressure

The mining time–pressure curves of each measuring point of coal seam roof during the test is shown in Fig. 14. During the mining process of working face X4, the pressure at all monitoring points fluctuates violently, showing a slight upward trend overall. With the mining of working face X3, the pressure at monitoring point 6 above the goaf gradually decreases, and the pressure at all monitoring points above the unmined coal seam increases slightly. When mining to working face X4 + 25 cm, the first large collapse of the roof is occurred, the pressure at the monitoring point 5 directly above the goaf decreases significantly, while the pressure at the monitoring point 4 above the coal pillar reaches the local pressure peak. When the mining of working face X3 is completed, the pressure at monitoring point 4, which is in the unloading area above the goaf, drops suddenly and obviously. While the pressure at monitoring point 3, which is close to the top of the coal pillar, starts to increase. It can be seen that the jump increase of pressure is caused by the fracture and collapse of the basic roof stratum, the fracture boundary and the supporting coal pillar are the main compression areas. Continuing mining to working face X3 + 17 cm, the roof collapses for the second time, but overburden does not contact with the caving zone, the pressure at monitoring points 4, 5 and 6 continues to decline. When mining to X3 + 34 cm, the roof collapses for the third time, resulting in the first integral bending subsidence of the slope, and overburden came into close contact with the caving zone locally. Since monitoring point 4 is near the contact area, its pressure increases sharply with the continuous compaction of the caving zone. Although monitoring points 3, 5 and 6 are also above the goaf, monitoring point 3 is closer to the fracture boundary on the stopping line side, while monitoring points 5 and 6 are closer to the fracture boundary on the open-off cut side. When mining to X3 + 41 cm and X2 + 25 cm, the pressure at monitoring points 2 and 1 appears local peaks respectively under the influence of leading abutment pressure, and then decreases substantially but does not drop to negative values. The pressure at monitoring point 1 is obviously larger than that of monitoring point 2, which indicates that the closer to the toe of the slope, the more obvious the phenomenon of compressive stress concentration is.

The large-scale change process of pressure in Fig. 14 basically corresponds to the position of initial weighting and periodic weighting in working face. The source of mine pressure lies in the process of the surrounding rock movement and deformation, such as microscopic damage, crack development, layer separation, fracture, rotary subsidence, and so on. During this period, the change and development of mining-induced stress of the roof have obvious time and space effects. The six monitoring points can be divided into two categories with the position of goaf as reference. Monitoring points 1, 2, 3 and 4 are located near the coal pillar ahead of working face advancing direction, and their pressure as well as the overburden deformation generally experiences the change process of increasing (leading abutment pressure action), substantial decreasing (roof separation or collapse), slightly increasing (slope subsiding and squeezing the caving zone) and maintaining stability (new stable state of rock mass structure). Among them, the pressure curve of monitoring point 4 shows a stepped growth, which is because monitoring point 4 is just located near the center line of slope settlement, coal seam roof collapses and the overburden sinking show periodic change characteristics, so the slope deformation is gradually intensified. Monitoring points 5 and 6 are close to the fracture boundary of the goaf, and their pressure and overburden deformation undergoes the change process of slightly increasing (leading abutment pressure action), decreasing (roof separation or collapse) and maintaining stable (stable rock mass structure in the fan-shaped fracture zone). By contrast, the closer to the boundary of the goaf on the open-cut side, the lower the pressure of the monitoring point is.

4.2.3 Variation Law of Overburden Displacement

Photographs of the deformation process of the model are processed to obtain the horizontal and vertical displacement nephograms of the overburden during the ascending mining, as shown in Figs. 15, 16, respectively. The meanings of positive and negative displacement values are referred to Sect. 4.1.3. The displacement data are likely to be missing in the areas where severe deformation occurs in the model, and are equally manifested in the displacement nephograms by equipotential lines mutation and grids deletion. The larger the excavation area of the coal seam working face, the more obvious the phenomenon of missing displacement data, such as the conical deformation area appearing in the displacement nephograms of Fig. 15g, h and Fig. 16g, h. Although the missing areas in the displacement nephograms are filled by the difference-completion hole method, the displacement values of the area are often too large and do not have statistical significance. Therefore, the overall deformation laws of the overburden are analyzed by the displacement nephograms only.

In the process of mining to X3 + 17 cm, coal seam roof collapses twice in a large area, and the overburden above the goaf and slope top have obvious deformation. The maximum
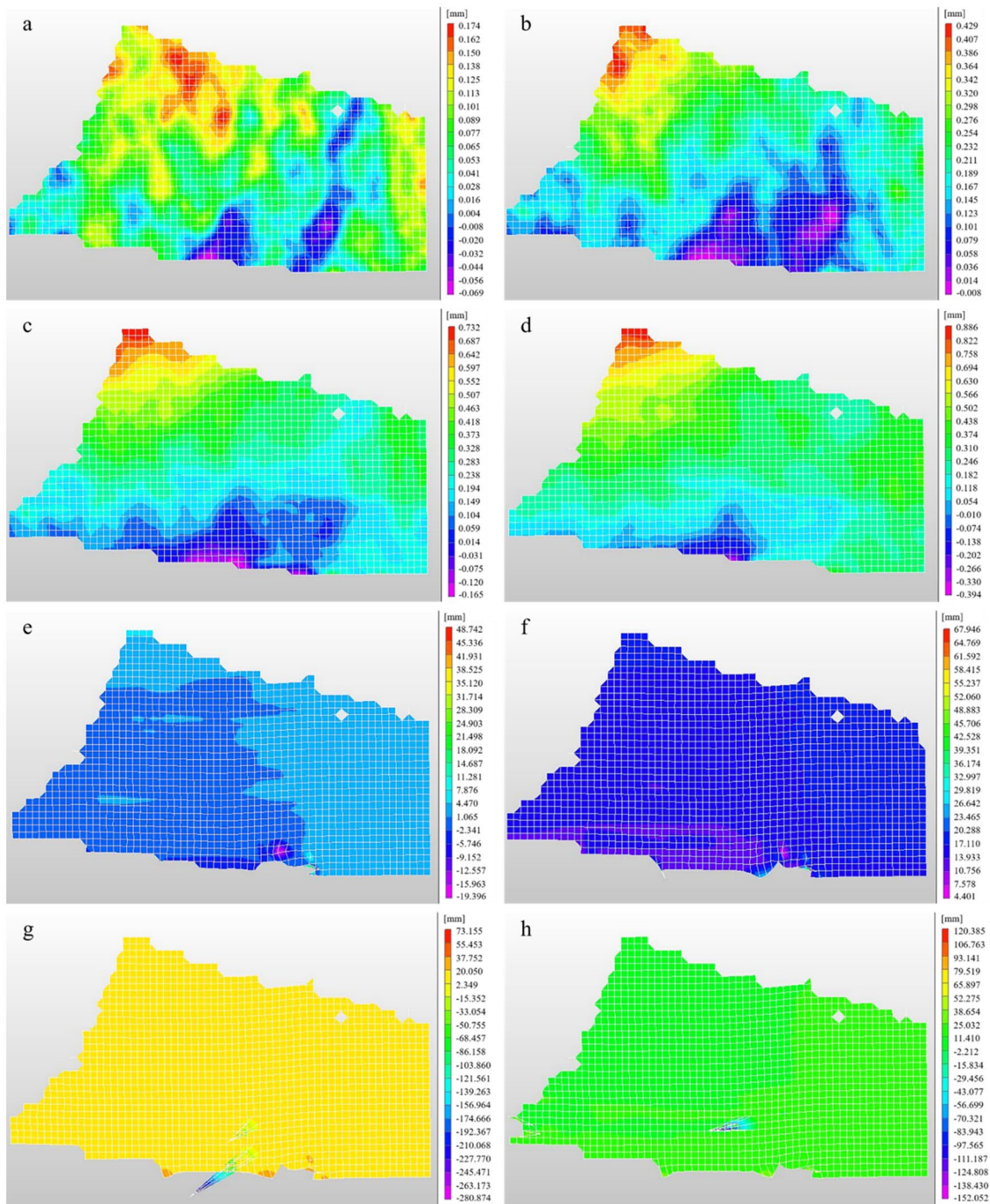
Fig. 15 Horizontal displacement nephograms of overburden in ascending mining: **a** excavation of X4; **b** excavation to X4 + 25 cm; **c** excavation of X3; **d** excavation to X3 + 17 cm; **e** excavation to X3 + 34 cm; **f** excavation of X2; **g** excavation to X2 + 25 cm; **h** excavation of X1

horizontal displacement of the slope top increases from 0.174 to 0.996 mm, with the displacement direction facing the inside of the slope. The maximum horizontal displacement and the maximum vertical displacement of the overburden above the goaf increases from −0.069, 0.615 to −0.394, 3.367 mm, with the displacement direction facing the free surface and downward respectively. It is generally

believed that due to the influence of roof bending subsidence and stratigraphic tilting, the shallow rock mass above the coal pillar in front of the ascending mining direction deforms toward the inside of the slope, while the deep rock mass above the coal pillar in front of the descending mining direction deforms toward the free surface (Wu et al. 2015; Yuan et al. 2016). Mining X3 + 17 cm to X3 + 34 cm section
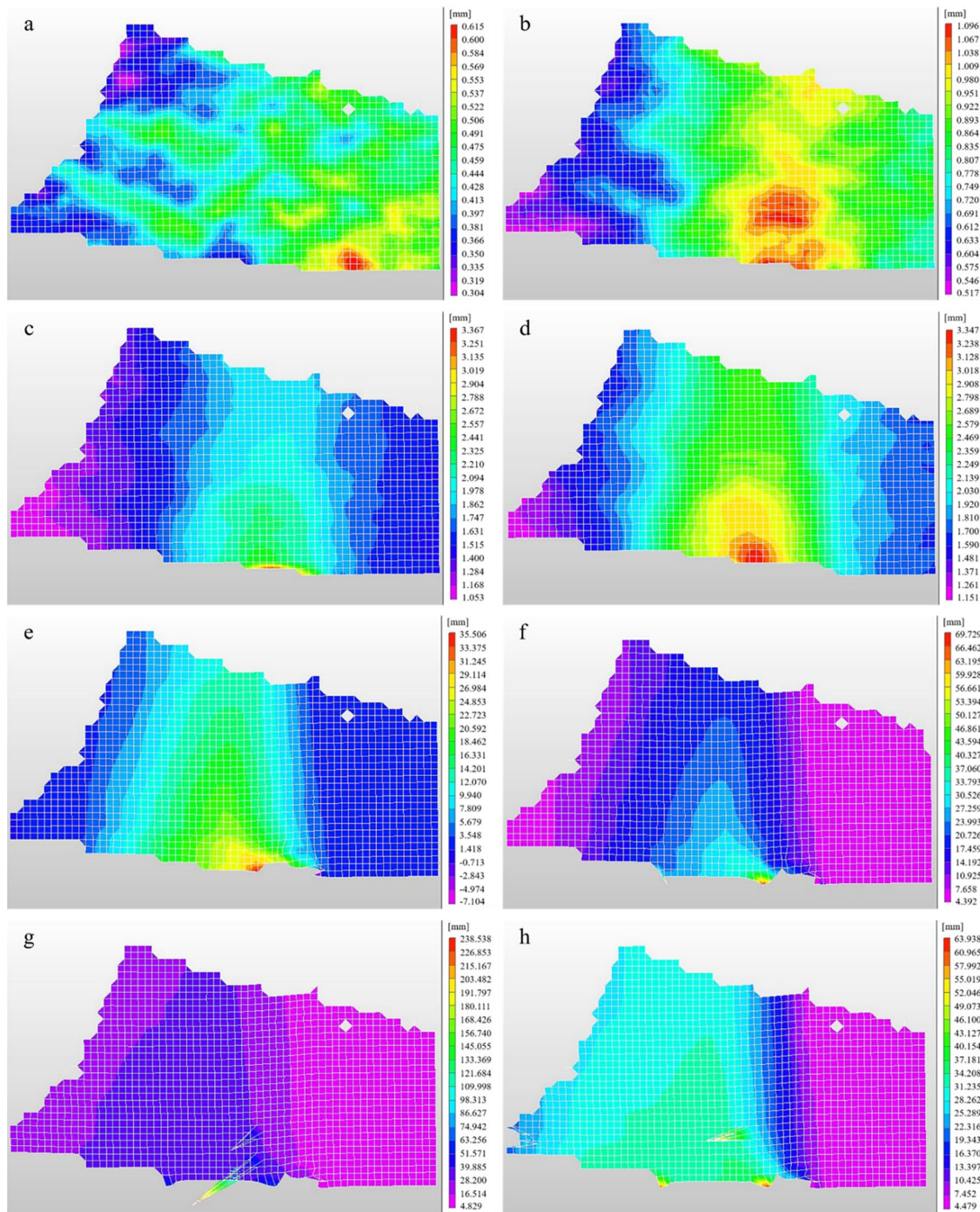
Fig. 16 Vertical displacement nephograms of overburden in ascending mining: **a** excavation of X4; **b** excavation to X4 + 25 cm; **c** excavation of X3; **d** excavation to X3 + 17 cm; **e** excavation to X3 + 34 cm; **f** excavation of X2; **g** excavation to X2 + 25 cm; **h** excavation of X1

of working face, the first integral bending subsidence of the slope occurs. The maximum horizontal displacement of the slope top rapidly increases to 11.281 mm, and the maximum horizontal displacement and maximum vertical displacement of the overburden above the goaf increases to −19.369 and 35.505 mm, respectively. At this time, the transverse deformation direction of slope top and the overburden above the

goaf is still opposite. During the process of mining face X1, the slope undergoes the second integral bending subsidence, and severe deformation toward the free surface occurs at the same time. Observing the equipotential lines in the vertical displacement nephogram, it can also be found that with the gradual mining of coal seam, the settlement center line of
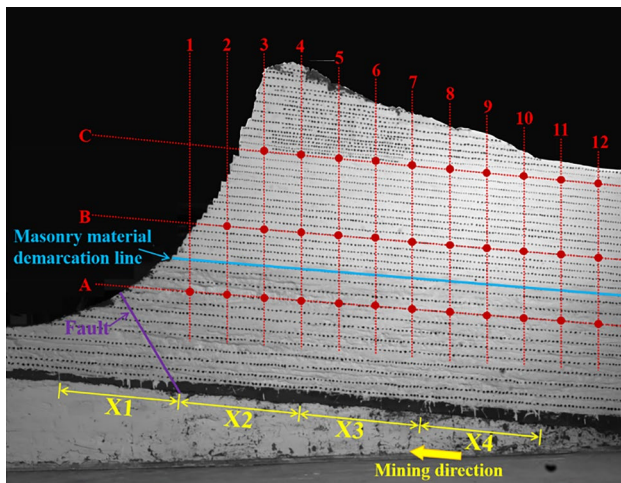
Fig. 17 Location of displacement monitoring lines and data points on overburden in ascending mining

the slope gradually shifts to the ascending mining direction and does not coincide with the midpoint line of the goaf.

Similarly, three transverse displacement monitoring lines and twelve columns of data points are extracted from the displacement nephograms to analyze the spatio-temporal variation of overburden deformation during mining. The specific location of the monitoring lines and data points is shown in Fig. 17.

In the process of mining to X3 + 17 cm, coal seam roof collapses twice, but a large-scale of fracture zone has not yet appeared on the overburden, and the moving process of the overburden is still in the stage of bending deformation and separation. It can be seen from Fig. 18 that before mining to X3 + 17 cm, the horizontal and vertical displacements of each data point on the three monitoring lines are extremely close, and the overburden undergoes minor deformation toward the inside of the slope and downward. Mining X3 + 17 cm to X3 + 34 cm section of working face, coal seam roof collapses once again, resulting in the first integral bending subsidence of the overburden. The horizontal and vertical displacements of all data points show a substantial surge. The horizontal displacement increment of data points A8–A12, B8–B12 and C8–C12 is the largest, but the vertical displacement increment is the smallest. When mining working face X1, the overburden occurs the second integral bending subsidence. Except for the increase of the horizontal displacements of data points A6 and A7, the horizontal displacements of other data points gradually decrease, and the horizontal displacements of data points on the three monitoring lines gradually decrease along the ascending mining direction. The vertical displacements of data points A1–A8, B2–B8 and C3–C8 increase significantly again, but the vertical displacements of data points A9–A12, B9–B12

and C9–C12 decrease slightly. The vertical displacements of data points C3–C5 is larger than that of data points B3–B5, which shows that the rock mass at the slope top already has the tendency of downward sliding, and the slope is prone to sliding instability.

Taking data points in 5th column with the largest vertical displacement as the dividing line, the vertical displacement gradually increases of data points in 1st columns to 4th column and decreases of data points in 6th column to 12th column. Referring to the position of the settlement center line of slope in Fig. 16, it is inferred that the position of data points in 5th column coincides with the settlement center line. During the first integral bending subsidence of the overburden, the vertical displacement variation rate gradually increases for data points in 1st columns to 4th column and decreases for data points in 6th column to 12th column. In the second integral bending subsidence of the overburden, the vertical displacement variation rate of data points in 1st columns to 12th column decreases gradually. It can be seen that the direct influence range of mining is distributed in an inverted trapezoid within the overburden, and the overburden that has been damaged above the mined workings is gradually tending to a new stable state.

5 Discussion of Collapse Processes and Failure Modes

5.1 Slope Failure Process and Mode in Descending Mining

Under the conditions of descending mining and ascending mining of coal seam, the failure mode for slope collapse is proposed and discussed, including the comprehensive deformation process at the scale of mine slopes over a large time span. It is based on geological analysis, field investigation and laboratory model experiment results. The failure process of slope is divided into four stages under coal seam descending mining conditions.

5.1.1 Coal Seam Roof Caving

After coal seam mining, the coal seam roof bends and fractures due to the loss of support, and slides and falls along the fault. Since the fault can block the influence of the caving of lower rock mass on the stability of the upper rock mass, the integral deformation of the slope is relatively small (Fig. 19a).
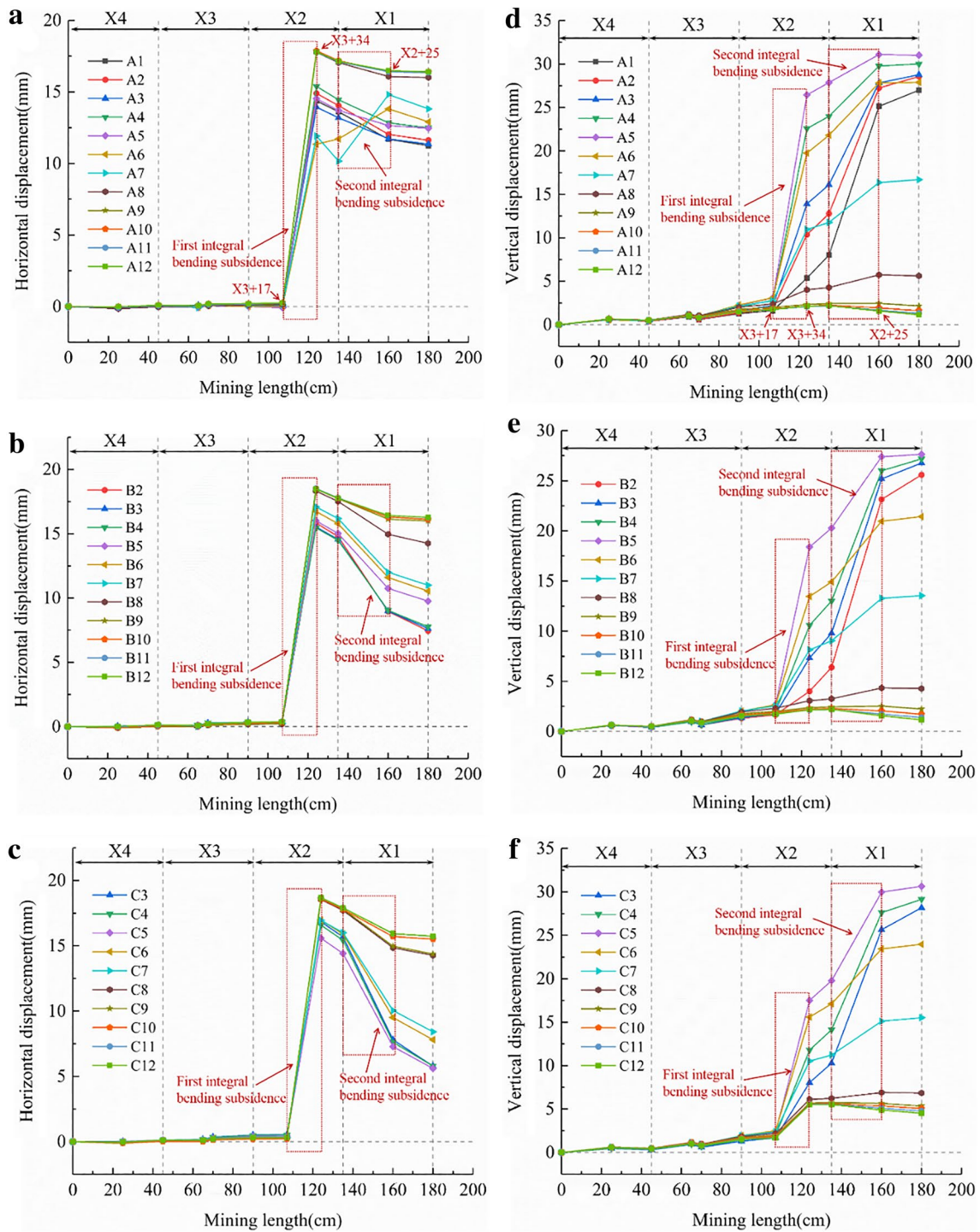
Fig. 18 Displacement variation curves of transverse monitoring lines in ascending mining: **a** horizontal displacement of line A; **b** horizontal displacement of line B; **c** horizontal displacement of line C; **d** vertical displacement of line A; **e** vertical displacement of line B; **f** vertical displacement of line C
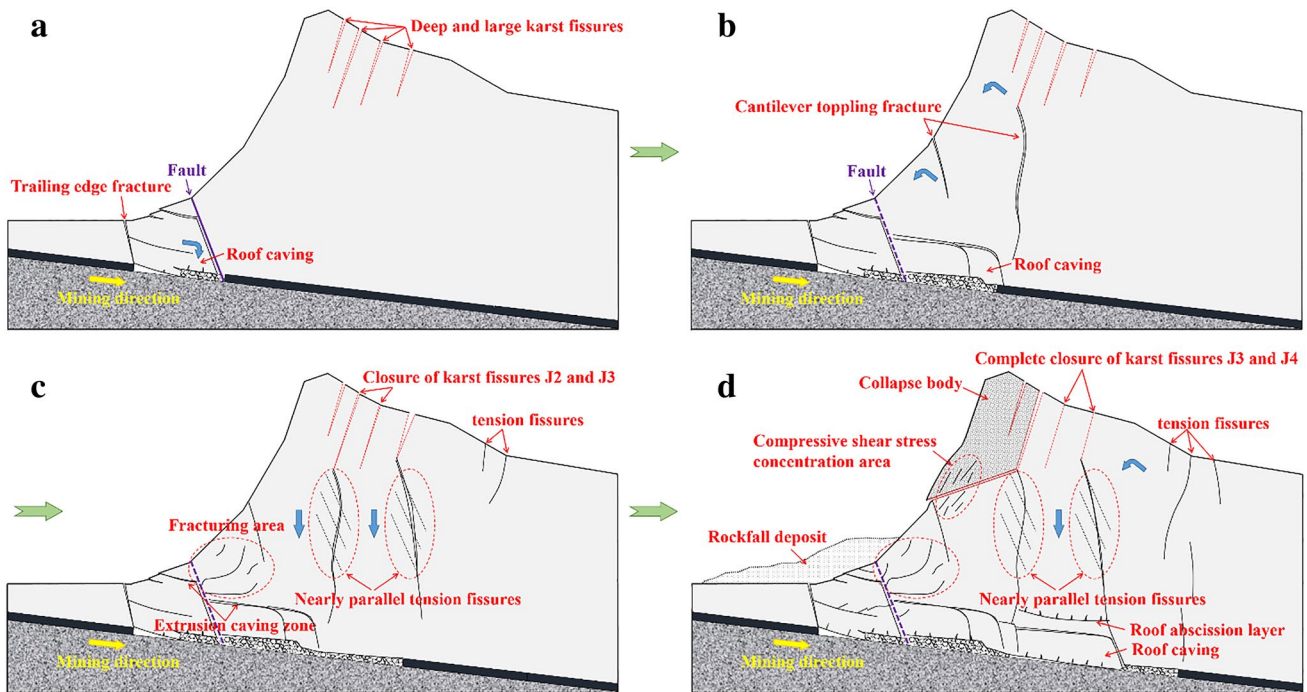
Fig. 19 Slope failure process under descending mining

5.1.2 Overburden Cantilever Tension Fracture

With the gradual mining of the coal seam, the goaf area gradually increases, and the hanging arch span of the roof gradually expands. The deformation of the roof is gradually transformed from elastic to plastic deformation, followed by periodic separation, fracture and caving on the roof, and the cantilever toppling fracture of the rock mass near the slope surface successively occurs toward the free surface. The existence of deep and large karst fissures at the slope top largely determines the extension direction of the tension cracks and the location of the slope body cracking, which plays a controlling role in the fracture failure of the cantilever structure and significantly destroys the integrity and stability of the slope (Fig. 19b).

5.1.3 Overburden Integral Dumping Subsidence

Under the influence of mining, the basic top rock layer evolves from a fractured state to a collapsed state (Liu et al. 2020). For thin coal seams, the fallen rock can fill the mine goaf, and the overburden can contact the fallen rock to form the extrusion caving zone (Egorov et al. 2001). When excavated to the middle of the slope, the slope undergoes a severe integral dumping subsidence, the caving zone and goaf are compacted. The originally opened cracks and the mined-out area are closed, and many compression–shear fissures appear

in the rock mass above the fault, which becomes a typical fracturing area (Fig. 19c).

5.1.4 Slope Instability Collapse

The tension fissures generally go through five stages: cracking, expansion, development to the maximum, beginning to close, and complete closure (Liu et al. 2019). The compression–shear failure area at the slope toe and the upper part of the slope gradually expand, and the soft–hard interbedded rock mass appears obvious bulging deformation, and finally is extruded. With the gradual penetration of compression–shear cracks and karst fissures at the shear outlet, the slope top rock mass will dump outward as a whole. Rock mass collapse occurs under suitable triggering mechanisms, such as precipitation, which causes the state of limiting equilibrium to be exceeded. The failure mode of the slope can be summarized as tension–shear–slip–toppling collapse failure (Fig. 19d).

5.2 Slope Failure Process and Mode in Ascending Mining

The slope failure process under the condition of coal seam ascending mining is also divided into four stages.
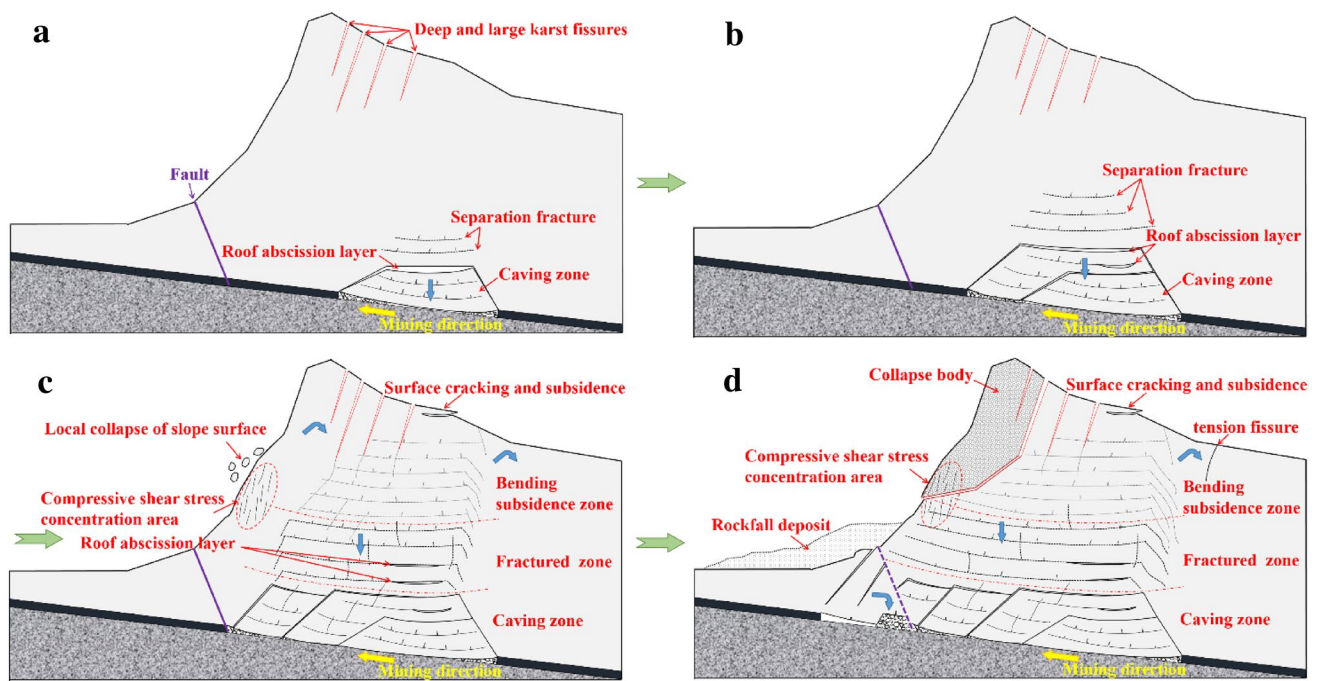
Fig. 20 Overburden failure process under ascending mining

5.2.1 Periodic Caving of Coal Seam Roof

The overburden is subject to the adjustment of stress due to the disturbance caused by the underground mining. In addition to the pre-existing unfavorable geological structure formed cumulatively in the past, (e.g., soft and hard interbedded rock structure) (Xu et al. 2016), the mining-induced stress and geometrical changes collectively caused the incipient deformation of the slope. The roof collapse in the early stage of coal seam mining does not seriously affect the overall stability of the slope (Fig. 20a).

5.2.2 Upward Transmission of Separation Fractures

The increase in the size of the mined-out area causes the periodic collapse of roof, which in turn leads to the formation of separation fractures. The fractures develop continuously along the horizontal and/or near-horizontal direction, transferring the goaf clearance space upward and forward within the overburden through the process of cracking, expansion, and closure (Fig. 20b).

5.2.3 Overburden Integral Bending Subsidence

When the coal seam is excavated for a long enough length, the overburden above the goaf will undergo the severe integral bending subsidence, and the overburden above the unmined coal seam will also occur a certain degree of

dumping and subsidence. The separation fractures within the slope gradually transfer to the surface, and the deep and large karst fissures continuously extend and expand downward. Cracking and subsidence are clearly visible on the surface, but the amount of surface subsidence is less than the height of the goaf, which is due to the separation fractures cause a certain spatial loss in the process of upward transmission (Singh and Singh 1999). Significant bulging of the slope surface, sporadic small-scale rock detachment and continuous rock falls can be observed during this phase. The bulge area is a compression–shear stress concentration area and the described phenomena indicate that the slope is likely to be at a state of limiting equilibrium (Fig. 20c).

5.2.4 Slope Instability Collapse

The deformation rate of cracks in the vertical and/or sub-vertical direction increases dramatically with more frequent small-scale rock detachments on the slope. The deep and large karst fissures at the slope top are important components of the potential collapse surface. The distance between the slope surface and the key karst fissure determines the final outcome of the failure mode. When the distance is small, it is easy to cause the bending motion of the rock mass toward the toe of slope, which consequently leads to the collapse of the slope (Zheng et al. 2015; Yin et al. 2020, 2021). The opening of karst fissures creates voids that can be filled by rock fragments and rainwater.

Consequently, the rainfall-induced static pore water pressures and seepage forces cause the rock mass to bend forward and in turn, the tension–shear–slip–toppling collapse failure to occur (Fig. 20d).

According to the previous video data taken by witnesses at the scene of the accident, Xiao et al. (2018) divided the failure process of the Pusa landslide into five stages: (1) deformation and collapse of the subsidence area; (2) local collapse of the slope surface; (3) complete collapse; (4) impacting the ground; and (5) formation of debris flow. The failure process of the slope under the descending and ascending mining conditions summarized by the test is consistent with the first three stages of the failure process of the Pusa landslide. Some critical phenomena are found in common for different mining conditions. For example, under descending and ascending mining conditions, the failure mode initiates from the crest or upper part of steep slopes with structurally decreasing strength from the upper to the lower strata. The final outcome of the failure modes is governed by the geological structures of the slope, e.g., the pre-existing vertical and/or sub-vertical joints. The existence of cracks and large mined-out area prerequisite for the slope deformation with all failure modes. The understanding of the geological structures provides a means for identifying the most likely failure mode for a potential collapse during the early stage.

5.3 Failure Conditions

Liu (2014) suggested that the formation and development of mining landslides should have three internal conditions: high and steep terrain, continuous mining history in the lower part of the mountain, and well-connected vertical joints in the mountain. The Pusha landslide fully meets the above conditions. The huge height difference and the mined-out

Fig. 21 Daily, monthly and cumulated rainfall preceding the landslide event recorded by the Zhangjiawan Town rainfall station. Collated from literature Fan et al. (2019)

area in the lower part of the mountain make the upper mountain form a structure similar to "cantilever beam" or "cantilever plate". The cutting action of joint fissures make rock mass easy to crack. In addition, water infiltration likely caused a build-up of hydrostatic pressures in the fractures and softened and weakened the siltstone and mudstone in the source mass, undermining slope stability (Zhang et al. 2016). After April 2017, Zhangjiawan Township, Nayong County, entered the stage of "prolonged sunshine and prolonged rain", of which late June and early mid-July were the rainy season, and the accumulated rainfall increased steeply from 147.9 mm on June 21 to 522.2 mm on July 21 (Fig. 21). Heavy rainfall is a direct trigger factor leading to the overall instability and failure of the mountain already in a critical state. The joint action of all above conditions breeds the occurrence of large-scale dangerous rock collapse.

5.4 Early Warning

In general, descending mining is the normal mining sequence with the advantages of simple mining, good safety, and convenient maintenance of roadway. While the shallow orebody with abundant reserves is mined in the early stage, deep exploration of the deposit can also be carried out. However, when the roof of the upper coal is hard and the coal seam is not easy to excavate, the gently inclined orebody can be mined by ascending mining. In addition, multi-seam mining under buildings and railways can be carried out by mining the lower coal seam first and the upper coal seam later to reduce the adverse effects of surface subsidence. The sudden increase of the coal seam roof pressure during descending mining and the substantial decrease and then increase of the roof pressure during ascending mining often indicate that the slope will be drastically deformed. Regardless of the mining method, any sudden acceleration in the horizontal and vertical displacement rate of the overburden is a critical sliding signal of the slope to forecast the occurrence of disaster risk. Based on this study of the Pusa landslide, local residents are advised to evacuate immediately to prevent potential life loss when small-scale rock detachments from the slopes with accelerated deformation.

Several cases demonstrated that, even though many geological disasters in mining areas occurred suddenly, several precursory signs can be identified. Therefore, it is certainly necessary to conduct in-depth investigation, continuous tracking and early warning of the geo-hazards in mining areas, especially in those with records of deformation signs and small failures. With the continuous development of monitoring technology, the level of geo-hazards monitoring has been significantly improved and perfected. Satellite remote sensing, InSAR technology and UAV remote sensing technology have the ability to identify regional deformation of geotechnical bodies well, and have a series of advantages, such as
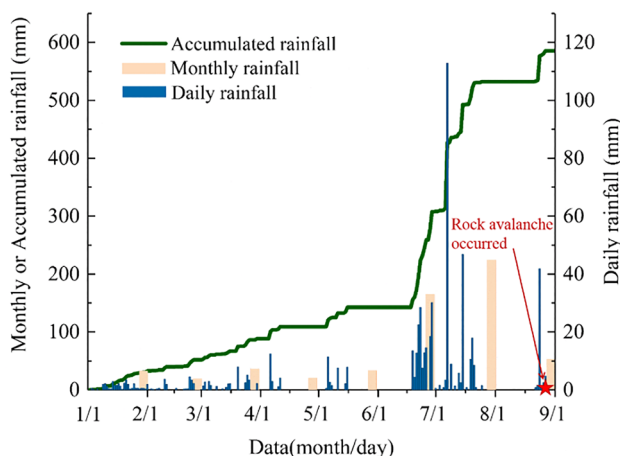
low monitoring cost, high map-forming efficiency and good accuracy of interpreted data, which are especially suitable for high-altitude areas, mountainous areas and environmentally vulnerable areas (Xu et al. 2017; Bekaert et al. 2020).

6 Conclusion

In this case study, the overburden movement feature and fracture evolution law under different mining methods were studied in light of the results from field investigation and physical model experiments. The pressure and displacement of overburden in the mining process were obtained by various means, such as soil pressure sensor, digital photography and non-contact 3D deformation measurement, and the variation laws of pressure and displacement were analyzed. The failure processes and failure modes of slope collapse controlled by deep and large karst fissures under the action of mining were proposed. The following main conclusions are drawn:

1. In the process of coal seam descending mining, the slope experiences four failure stages: coal seam roof caving, overburden cantilever tension fracture, overburden integral dumping subsidence and slope instability collapse, and the slope undergoes deformation toward the free surface and downward. During the ascending mining process, the slope also experiences four failure stages: periodic caving of coal seam roof, upward transmission of separated fractures, overburden integral bending subsidence and slope instability collapse, and the slope undergoes deformation toward the inside of the slope and downward.
2. The tension cracks generally go through five stages: cracking, expansion, development to the maximum, beginning to close, and complete closure. Separation fractures transfer the goaf clearance space upward and forward within the overburden through the process of cracking, expansion, and closure.
3. The rock mass ahead of the advancing direction of working face has the phenomenon of tension–compression stress transformation. Along the mining direction, the overburden sequentially experiences the change process of pressure increase, decrease, or increase again, and stabilization.
4. The existence of deep and large karst fissures at the top of the slope largely determines the extension direction of the tension cracks and the location of the slope body cracking, which play a controlling role in the fracture failure of the cantilever structure and are important components of the potential collapse surface. The failure mode of slope controlled by deep and large karst

fissures under the action of mining can be summarized as tension–shear–slip–toppling collapse failure.

Declarations

References

Bekaert DPS, Handwerger AL, Agram P, Kirschbaum DB (2020) InSAR-based detection method for mapping and monitoring slow-moving landslides in remote regions with steep and mountainous terrain: an application to Nepal. Remote Sens Environ 249(1):111983. https://doi.org/10.1016/j.rse.2020.111983

Benko B, Stead D (1998) The Frank slide: a reexamination of the failure mechanism. Can Geotech J 35(2):299–311. https://doi.org/10.1139/t98-005

Bentley SP, Siddle HJ (1996) Landslide research in the South Wales coalfield. Eng Geol 43(1):65–80. https://doi.org/10.1016/0013-7952(95)00084-4

Capparelli G, Damiano E, Greco R, Olivares L, Spolverino G (2019) Physical modeling investigation of rainfall infiltration in steep layered volcanoclastic slopes. J Hydrol 580:124199. https://doi.org/10.1016/j.jhydrol.2019.124199

Chen SJ, Li YY, Guo WJ, Lu C, Wang HY, Yin DW (2015) Similar materials of colliery filling for physical simulation experiment. Mater Res Innov 19(S5):S5-304-S5-307. https://doi.org/10.1179/1432891714Z.0000000001098

Chen L, Fan SW, Zhao C, Zhang L, Cheng ZH (2019) Calculation method of overburden damage height based on fracture mechanics analysis of soft and hard rock layers. Geofluids 2019:1–15. https://doi.org/10.1155/2019/3790264

Chen L, Zhao C, Li B, He K, Ren C, Liu X, Liu D (2021) Deformation monitoring and failure mode research of mining-induced Jianshanying landslide in karst mountain area, China with ALOS/PALSAR-2 images. Landslides 18:2739–2750. https://doi.org/10.1007/s10346-021-01678-6

Cui FP, Li B, Xiong C, Yang ZP, Peng JQ, Li JS, Li HW (2022) Dynamic triggering mechanism of the Pusa mining-induced landslide in Nayong County, Guizhou Province, China. Geomat Nat Haz Risk 13(1):123–147. https://doi.org/10.1080/19475705.2021.2017020

Cunningham DM (1988) A rockfall avalanche in a sandstone landscape, Nattai North, NSW. Australian Geogr 19(2):221–229. https://doi.org/10.1080/00049188808702961

Do TN, Wu JH (2019) Simulating a mining-triggered rock avalanche using DDA: a case study in Nattai North, Australia. Eng Geol 264:105386. https://doi.org/10.1016/j.enggeo.2019.105386

Do TN, Wu JH (2020a) Simulation of the inclined jointed rock mass behaviors in a mountain tunnel excavation using DDA. Comput Geotech 117:103249. https://doi.org/10.1016/j.compgeo.2019.103249

Do TN, Wu JH (2020b) Verifying discontinuous deformation analysis simulations of the jointed rock mass behavior of shallow

twin mountain tunnels. Int J Rock Mech Min Sci 130(2):104322. https://doi.org/10.1016/j.ijrmms.2020.104322

Du WG, Chai J, Zhang DD, Lei WL (2021) Application of optical fiber sensing technology in similar model test of shallow-buried and thick coal seam mining. Measurement 191(3):109559. https://doi.org/10.1016/J.MEASUREMENT.2021.109559

Eberhardt E, Thuro K, Luginbuehl K (2005) Slope instability mechanisms in dipping interbedded conglomerates and weathered marls-the 1999 Rufi landslide, Switzerland. Eng Geol 77(1–2):35–56. https://doi.org/10.1016/j.enggeo.2004.08.004

Egorov PV, Kalinin SI, Agudalin BP (2001) Technological and geomechanical parameters of room-and-pillar system of mining a thick flat seam. J Min Sci 37(5):472–474. https://doi.org/10.1023/A:1015166906969

Erginal AE, Türkeş M, Ertek TA, Baba A, Bayrakdar C (2008) Geomorphological investigation of the excavation-induced Dündar Landslide, Bursa-Turkey. Geogr Ann Ser B 90(2):109–123. https://doi.org/10.2307/40204885

Fan XM, Xu Q, Scaringi G, Zheng G, Huang RQ, Dai LX, Ju YZ (2019) The "long" runout rock avalanche in Pusa, China, on August 28, 2017: a preliminary report. Landslides 16:139–154. https://doi.org/10.1007/s10346-018-1084-z

Feng Z, Li B, Cai QP, Cao JW (2016) Initiation Mechanism of the Jiweishan Landslide in Chongqing, Southwestern China. Environ Eng Geosci 22(4):341–351. https://doi.org/10.2113/gseegeosci.22.4.341

Fernández PR, Granda GR, Krzemień A, Cortés SG, Valverde GF (2020) Subsidence versus natural landslides when dealing with property damage liabilities in underground coal mines. Int J Rock Mech Min 126:104175. https://doi.org/10.1016/j.ijrmms.2019.104175

Ghadafi MA, Toha MT, Setiabudidaya D (2017) Effect of ground vibration to slope stability, case study landslide on the mouth of railway tunnel Gunung Gajah Village Lahat District. Sriwijaya J Environ 2(3):67–71. https://doi.org/10.22135/sje.2017.2.3.67-71

He K, Gao Y, Wang WP, Zhu SN (2018) Physical model experimental study on deformation and failure of overlying rock slope under the condition of steep coal seam mining. J Geomech 24(3):399–406 (**in Chinese**)

Hu XL, He CC, Zhou C, Xu C, Zhang H, Wang Q, Wu SS (2019) Model test and numerical analysis on the deformation and stability of a landslide subjected to reservoir filling. Geofluids. https://doi.org/10.1155/2019/5924580

Kratcsch H (1986) Mining subsidence engineering. Environ Geol 8(3):133–136. https://doi.org/10.1007/bf02509900

Lana MS (2014) Numerical modeling of failure mechanisms in phyllite mine slopes in Brazil. Int J Min Sci Technol 24(6):777–782. https://doi.org/10.1016/j.ijmst.2014.10.007

Li B, Feng Z, Wang GZ, Wan WP (2016) Processes and behaviors of block topple avalanches resulting from carbonate slope failures due to underground mining. Environ Earth Sci 75(8):694. https://doi.org/10.1007/s12665-016-5529-1

Li Y, Wang JP, Chen YD, Lei MX, Yang DP, Yang KP, Yuan YH (2020) Study on effect of interburden on movement of overburden in multiple coal seams. Coal Sci Technol 48(4):246–255 (**in Chinese**)

Liao Z, Feng T, Yu WJ, Wu GS, Li K, Gong FQ (2020) Experimental and theoretical investigation of overburden failure law of fully mechanized work face in steep coal seam. Adv Civil Eng 4:1–10. https://doi.org/10.1155/2020/8843172

Lin F, Wu LZ, Huang RQ, Zhang H (2018) Formation and characteristics of the Xiaoba landslide in Fuquan, Guizhou, China. Landslides 15(2):669–681. https://doi.org/10.1007/s10346-017-0897-5

Liu TQ (1995) Influence of mining activities on mine rockmass and control engineering. J China Coal Soc 20(1):1–5 (**in Chinese**)

Liu CZ (2014) Genetic types of landslide and debris flow disasters in China. Geol Rev 60(4):858–868

Liu QC, Xiong CR, Ma JW (2015) Study of Guizhou Province Guanling Daz-Hai landslide instability process under the rainstorm. Appl Mech Mater 733:446–450. https://doi.org/10.4028/www.scientific.net/AMM.733.446

Liu H, Deng KZ, Zhu XJ, Jiang CL (2019) Effects of mining speed on the developmental features of mining-induced ground fissures. Bull Eng Geol Env 78:6297–6309. https://doi.org/10.1007/s10064-019-01532-z

Liu WT, Pang LF, Xu BC, Sun X (2020) Study on overburden failure characteristics in deep thick loose seam and thick coal seam mining. Geomat Nat Haz Risk 11(1):632–653. https://doi.org/10.1080/19475705.2020.1737584

Lu GZ, Tang JQ, Song ZQ (2010) Difference between cyclic fracturing and cyclic weighting interval of transferring rock beams. Chinese J Geotech Eng 32(4):538–541 (**in Chinese**)

Ma GT, Hu XW, Yin YP, Luo G, Pan YX (2018) Failure mechanisms and development of catastrophic rockslides triggered by precipitation and open-pit mining in Emei, Sichuan, China. Landslides 15:1401–1414. https://doi.org/10.1007/s10346-018-0981-5

Ma CQ, Yuan YF, Zha JL, Li HZ, Xu YY (2020) Determine method of effective experimental period of similar material model for improving the simulation results. Energy Sources A Recov Utilization Environ Effects. https://doi.org/10.1080/15567036.2020.1815909

Nie L, Li ZC, Zhang M, Xu LN (2015) Deformation characteristics and mechanism of the landslide in West Open-Pit Mine, Fushun China. Arab J Geosci 8(7):57–68. https://doi.org/10.1007/s12517-014-1560-2

Ning JG, Wang J, Tan YL, Xu Q (2019) Mechanical mechanism of overlying strata breaking and development of fractured zone during close-distance coal seam group mining. Int J Min Sci Technol 30(2):207–215. https://doi.org/10.1016/j.ijmst.2019.03.001

Ouyang G, Lan ZX (2009) Construction report design of collapse geological hazard treatment project of Pusa coal mine in Zhangjiawan town, Nayong County. Guizhou Dikuang Engineering Investigation Corporation, Guiyang (**in Chinese**)

Palchik V (2005) Localization of mining-induced horizontal fractures along rock layer interfaces in overburden: field measurements and prediction. J Environ Geol 48:68–80. https://doi.org/10.1007/s00254-005-1261-y

Palchik V (2015) Bulking factors and extents of caved zones in weathered overburden of shallow abandoned underground workings. J Int J Rock Mech Min Sci 79:227–240. https://doi.org/10.1016/j.ijrmms.2015.07.005

Salmi EF, Nazem M, Karakus M (2017) Numerical analysis of a large landslide induced by coal mining subsidence. Eng Geol 217:141–152. https://doi.org/10.1016/j.enggeo.2016.12.021

Scaringi G, Fan XM, Xu Q, Liu C, Ouyang CJ, Domènech G, Yang F, Dai LX (2018) Some considerations on the use of numerical methods to simulate past landslides and possible new failures: the case of the recent Xinmo landslide (Sichuan, China). Landslides 15(7):1359–1375. https://doi.org/10.1007/s10346-018-0953-9

Sebastian W, Peter T, James H (2014) New insights into the emplacement dynamics of volcanic island landslides. Oceanography 27(2):46–57. https://doi.org/10.5670/oceanog.2014.39

Singh R, Singh TN (1999) Wide stall mining for optimal recovery of coal from a thick seam under surface features. Int J Rock Mech Min Sci 36(2):155–168. https://doi.org/10.1016/s0148-9062(98)00177-6

Singhal BBS, Gupta RP (1999) Fractures and discontinuities. In: Singhal BBS, Gupta RP (eds) Applied hydrogeology of fractured rocks. Springer, Dordrecht, pp 13–35. https://doi.org/10.1007/978-94-015-9208-6_2

Sun Y, Yao B (1983) Research on failure mechanism of rockfall in Yanchi River phosphorite. Hydrogeol Eng Geol 1–7 (**in Chinese**)

Tangri A, Rawat S (2021) Soil nails for slope reinforcement: a lab-based model study. Mater Today Proc 1:728

Tao X, Tian H, Yang C (2015) Mining induced strata movement and roof behavior in underground coal mine. Geomech Geophys Geo-Energy Geo-Resour 1:79–89. https://doi.org/10.1007/s40948-015-0010-2

Tao ZG, Shu Y, Yang XJ, Peng YY, Chen QH, Zhang HJ (2020) Physical model test study on shear strength characteristics of slope sliding surface in Nanfen open-pit mine. Int J Min Sci Technol 3:421–429. https://doi.org/10.1016/j.ijmst.2020.05.006

Unrug K, Szwilski TB (1982) Methods of roof caveability prediction. State of the art of ground control in longwall mining and mining subsidence. AIME, New York, pp 13–29

Valentin G, Giona P, Erik E (2016) Numerical investigation of seismically induced rock mass fatigue as a mechanism contributing to the progressive failure of deep-seated landslides. Rock Mech Rock Eng 49(6):2457–2478. https://doi.org/10.1007/s00603-015-0821-z

Wang C, Zhang NC, Han YF, Xiong ZQ, Qian DY (2015) Experiment research on overburden mining-induced fracture evolution and its fractal characteristics in ascending mining. Arab J Geosci 8(1):13–21. https://doi.org/10.1007/s12517-013-1178-9

Wang HW, Xue S, Shi RM, Jiang YS, Gong WL, Mao LT (2019) Investigation of fault displacement evolution during extraction in longwall panel in an underground coal mine. Rock Mech Rock Eng 53(10):1809–1826. https://doi.org/10.1007/s00603-019-02015-z

Wang HW, Shi RM, Deng DX, Jiang YD, Wang G, Gong WL (2020) Characteristic of stress evolution on fault surface and coal bursts mechanism during the extraction of longwall face in Yima mining area, China. J Struct Geol 136(1):104071. https://doi.org/10.1016/j.jsg.2020.104071

Wu JH, Ohnishi Y, Nishiyama S (2004) Investigation on block displacements due to a shallow tunnel excavation in an inclined brick-type jointed rock mass using discontinuous deformation analysis. J Chin Inst Eng 27(3):307–314. https://doi.org/10.1080/02533839.2004.9670878

Wu K, Cheng GL, Zhou DW (2015) Experimental research on dynamic movement in strata overlying coal mines using similar material modeling. Arab J Geosci 8(9):6521–6534. https://doi.org/10.1007/s12517-014-1685-3

Wu LZ, Zhou Y, Sun P, Shi JS, Liu GG, Bai LY (2017) Laboratory characterization of rainfall-induced loess slope failure. CATENA 150:1–8. https://doi.org/10.1016/j.catena.2016.11.002

Wu QS, Jiang LS, Wu QL, Xue YC, Gong B (2018) A study on the law of overlying strata migration and separation space evolution under hard and thick strata in underground coal mining by similar simulation. DYNA 94(1):175–181. https://doi.org/10.6036/8678

Xiao RH, Chen HQ, Leng YY, Wei YJ, Wang WP (2018) Preliminary analysis on the failure process and mechanism of the August 28 collapse in Nayong County, Guizhou Province. Chin J Geol Hazard Control 29(1):3–9 (**in Chinese**)

Xu Q, Liu H, Ran J, Li W, Sun X (2016) Field monitoring of groundwater responses to heavy rainfalls and the early warning of the Kualiangzi landslide in Sichuan Basin, southwestern China. Landslides 13(6):1555–1570. https://doi.org/10.1007/s10346-016-0717-3

Xu Q, Li WL, Dong XJ, Xiao XX, Fan XM, Pei XJ (2017) The Xinmocun landslide on June 24, 2017 in Maoxian, Sichuan: characteristics and failure mechanism. Chin J Rock Mech Eng 36(11):2612–2628 (**in Chinese**)

Xue JH, Wang HP, Zhou W, Ren B, Duan CR, Deng DS (2015) Experimental research on overlying strata movement and fracture evolution in pillarless stress-relief mining. Int J Coal Sci Technol 2(1):38–45. https://doi.org/10.1007/s40789-015-0067-0

Yang ZP, Jiang YW, Li B, Gao Y, Liu XR, Zhao YL (2020) Study on the mechanism of deep and large fracture propagation and transfixion in karst slope under the action of mining. J Geomech 26(4):459–470 (**in Chinese**)

Yin YP, Liu CZ, Chen HQ, Ren J, Zhu CB (2013) Investigation on catastrophic landslide of January 11, 2013 at Zhaojiagou, Zhenxiong county, Yunnan province. J Eng Geol 21(1):6–15 (**in Chinese**)

Yin ZM, Liu XR, Yang ZP, Jiang YW, Zhao YL, Li SQ (2020) Shear characteristics and failure mode of hard brittle marl with parallel discontinuous structural plane. Arab J Sci Eng 45:8219–8229. https://doi.org/10.1007/s13369-020-04674-5

Yin ZM, Liu XR, Yang ZP, Wang YL (2021) Shear behavior of marlstone containing parallel fissure under normal unloading. KSCE J Civ Eng 25:1283–1294. https://doi.org/10.1007/s12205-021-0959-z

Yu F, Liu SQ, Xu YC, Zhao L (2020) Failure analysis of thin bedrock and clay roof in underground coal mining: case study in Longdong coal mine. Int J Geomech 20(10):04020187. https://doi.org/10.1061/(ASCE)GM.1943-5622.0001839

Yuan AY, Zhang ZQ, Li Y (2016) Study on the influence rule of underlying working face to overlying rock and high level tunnel. In: Proceedings of the 2015 2nd international conference on machinery, materials engineering, chemical engineering and biotechnology. https://doi.org/10.2991/mmeceb-15.2016.169

Zhang S, Xu Q, Hu Z (2016) Effects of rainwater softening on red mudstone of deepseated landslide, Southwest China. Eng Geol 204:1–13. https://doi.org/10.1016/j.enggeo.2016.01.013

Zhang Y, Cao SG, Guo SA, Wan T, Wang JJ (2018a) Mechanisms of the development of water-conducting fracture zone in overlying strata during shortwall block backfill mining: a case study in Northwestern China. Environ Earth Sci 77(14):543. https://doi.org/10.1007/s12665-018-7726-6

Zhang YQ, Tang HM, Li CD, Lu GY, Cai Y, Zhang JR, Tan FL (2018b) Design and testing of a flexible inclinometer probe for model tests of landslide deep displacement measurement. Sensors 18(1):224. https://doi.org/10.3390/s18010224

Zheng D, Frost JD, Huang RQ, Liu FZ (2015) Failure process and modes of rockfall induced by underground mining: a case study of Kaiyang phosphorite mine rockfalls. Eng Geol 197:145–157. https://doi.org/10.1016/j.enggeo.2015.08.011

Zhong ZL, Wang NY, Li B, Liu XR, Cui FP, Yang ZP (2020) Experimental study on the deformation mechanism of upper-hard and lower-soft gently dipping rock on high slopes under the mining effect. Carsolog Sin 39(4):509–517 (**in Chinese**)

Zhou D, Ye YC, Hu NY, Wang WQ, Wang XH (2021) Crack evolution of soft-hard composite layered rock-like specimens with two fissures under uniaxial compression. Front Struct Civ Eng 15:1372–1389. https://doi.org/10.1007/s11709-021-0772-2